Journal of Materials Chemistry A

ROYAL SOCIETY OF CHEMISTRY

REVIEW

View Article Online
View Journal | View Issue

Cite this: J. Mater. Chem. A, 2022, 10, 19320

Metal–organic frameworks based on infinite secondary building units: recent progress and future outlooks

Jun Guo, *[a] Xiaomin Xue,[a] Haibin Yu,[b] Yulong Duan,[a] Fangfang Li,[a] Ye Lian,[a] Yi Liu *[a] and Meiting Zhao *[c]

Received 20th April 2022
Accepted 26th June 2022

DOI: 10.1039/d2ta03159k

rsc.li/materials-a

Metal–organic frameworks (MOFs) are a type of inorganic–organic hybrid connected by organic ligands and discrete metal ions/metallic secondary building units (SBUs). Recently, more and more MOF examples based on infinite SBUs (ISBUs) including one-dimensional (1D) rods, two-dimensional (2D) sheets, and even three-dimensional (3D) nets have emerged and exhibited unique physical and chemical properties (*e.g.*, excellent stability, strong light absorption, and fast charge carrier mobility). Hence, rapidly increasing endeavors have been devoted to the structure design, synthesis methodology, property exploration and performance evaluation of novel ISBU MOFs. In this timely review, we will first summarize the established synthesis methods and resolved crystallographic structures of various types of ISBU MOFs. At the same time, the distinct physical and chemical properties resulting from corresponding ISBUs deserve to be highlighted and compared with traditional MOFs consisting of discrete metal ions/SBUs. Moreover, recent progress of those ISBU MOFs achieved in fields of gas adsorption and separation, energy conversion, photocatalysis, *etc.* is also introduced. We hope it is constructive and attractive for further advancement achieved in this new but intriguing research field.

1. Introduction

Metal–organic frameworks (MOFs) have become a new class of porous materials and have attracted substantial attention in various fields[1–6] thanks but not limited to their large surface area, high porosity, and versatile tunability.[7–11] In most cases, the metal ions or metallic secondary building units (SBUs) are considered as discrete zero-dimensional (0D) nodes that are further linked by organic ligands for the construction of frameworks.[12–15] Distinctly, infinite SBUs (ISBUs) like one-dimensional (1D) chains,[16–18] two-dimensional (2D) sheets,[19–21] and even three-dimensional (3D) nets[22–24] have also emerged in MOFs and been rapidly developed recently. Consequently, MOFs can also be categorized into OD, 1D, 2D, and 3D subclasses according to the ISBU types (Scheme 1). On account of the pure inorganic metal-oxo nature in one dimension at least, ISBU MOFs resemble the corresponding metal oxides/metal hydroxides in terms of physical and chemical properties (*e.g.*, excellent stability, high carrier mobility and dense unit package).[21,25–27] To a certain degree, ISBU MOFs can be even considered as special assemblies of metal-oxide/hydroxide nanostructures (*e.g.* nanowires, nanosheets and nano-frames) and organic linkers. As a result, exceptional performances of ISBU MOFs have been achieved in application fields of adsorption,[3,28,29] gas separation,[30,31] energy conversion,[27,32] biomaterial[33] and photocatalysis.[34,35] For instance, the 1D chain-like Al-MOF reported the recent state-of-the-art water-harvesting

[a]State Key Laboratory of Separation Membranes and Membrane Processes, School of Chemistry, Tiangong University, Tianjin 300387, China. E-mail: junguo@tiangong.edu.cn; yiliuchem@whu.edu.cn

[b]CenerTech Tianjin Chemical Research & Design Institute Co., Ltd, Tianjin 300131, China

[c]Tianjin Key Laboratory of Molecular Optoelectronic Sciences, Department of Chemistry, Institute of Molecular Aggregation Science, Tianjin University, Tianjin 300072, China. E-mail: mtzhao@tju.edu.cn

Meiting Zhao obtained his Ph.D. degree from National Center for Nanoscience and Technology in 2014 under the guidance of Prof. Zhiyong Tang. Then he worked as a postdoctoral research fellow in Prof. Hua Zhang's group in Nanyang Technological University. In 2019, he joined Tianjin University as a professor. His research interests include the structure design, controlled synthesis and application of MOFs, COFs and their composites in selective catalysis, separation and energy conversion.

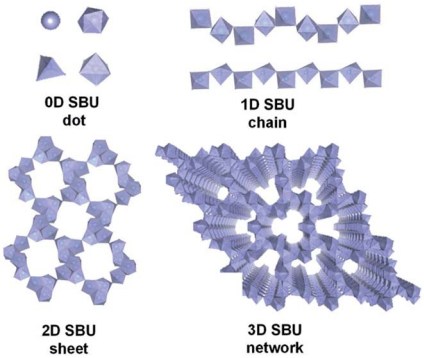

Scheme 1 The categorization of MOFs according to their SBU types.

uptake, thanks to its unique channels embraced by the hydrophilic Al–O chains along with polar linkers.[3] Moreover, the densely stacking of linkers enforced by 1D MOFs is beneficial for commanding multivariate active sites working in a synergistic way, which is essential to achieve excellent catalytic activity[32] and even specific selectivity.[30] Analogous to inorganic semiconductor nanomaterials, ISBU MOFs can even exhibit nearly identical energy band structure and comparable even surpassed carrier mobility, as demonstrated in the case of some Ti-MOFs constituted of infinite Ti–O chains[18,35–37] and sheets.[19] Last but not least, ISBU MOFs are expected to inherit the robust physical and chemical stabilities of corresponding metal inorganics, which are crucial for maintaining long-term performances in various application fields, especially in catalysis.[17,38]

In this review, we will first comprehensively introduce the synthesis and crystal structure of ISBU MOFs according to their central metallic valence states. In order to give a clear and straightforward illustration, many crystallographic structures of ISBU MOFs have been redepicted on basis of the reported crystallographic information files.[39,40] However, considering the enormous number of examples, especially 1D MOFs reported so far, only the recently developed or prototype ones are presented in this review, readers who are interested in a more comprehensive summary of 1D MOFs reported before 2017 can refer to another review.[41] Secondly, we are going to discuss the performances of ISBU MOFs in versatile fields including gas adsorption, gas separation, energy-related applications and catalysis with attempts to highlight the roles of corresponding ISBU structures. Last, the existing challenges and future outlooks in this infancy but intriguing research field are also proposed based on our personal insights. It is hoped that this review will be constructive and attractive for achieving further advancement for ISBU MOFs in the near future.

2. ISBU MOFs

According to the basic principle of coordination chemistry, the structure type of ISBU among MOFs depends on the coordination mode (*e.g.*, coordination number, geometry pattern and bonding strength) of the central metal ion crucially, which is also related to its bonding orbitals, carried charges, ionic radius and so on. Attempt to give a clear representation to authors, the introduction of each type of ISBU (*e.g.*, 1D, 2D and even 3D) MOFs in this review has been further arranged by the valent state of central metals mainly.

2.1 ISBU MOFs constituted of metal(I) central ions

In 2019, Davies *et al.*[42] reported a series of 1D MOFs based on Li^+ and Na^+ metal centers using silane-based organic linkers. For example, the 1D Li-MOF [IMP-24Li, $Li_4L1\cdot DMF$, in which L1 = 4,4′,4′′-(methylsilanetriyl)tribenzoate] was synthesized by mixing lithium nitrate ($LiNO_3$) and H_3L1 in DMF at the reaction temperature of 170 °C. IMP-24Li crystallized in a unique chiral space group of $P3_121$, wherein each unit cell contained one L1 ligand, four lithium cations, and one coordination DMF molecule. Caused by the positional disorders within the unit cell, the detailed coordination of IMP-24Li was unable to be accurately measured. Nevertheless, the 1D helical Li–O chain with a pitch of 1.64 nm (Fig. 1a) has been unambiguously observed, which was further linked with each other by L1 bridging linkers to form the open 3D IMP-24 framework (Fig. 1b). Furthermore, the 1D Na-MOF named as IMP-27Na $[Na_4(L2)(H_2O)_4(DMF)_4$, in which L2 = 4,4′,4″,4‴-silanetetrayltetrabenzoate] was synthesized by mixing $NaNO_3$ and H_4L2 in DMF at 170 °C. Differently, IMP-27Na crystallized in a triclinic system with the $P\bar{1}$ space group, in which there were four sodium ions, one L1 ligand, four coordinated DMF molecules, and additional two water molecules. Fortunately, the 1D Na–O chain in IMP-27Na has been successfully resolved by single-crystal X-ray diffraction measurement, which was composed of repeat asymmetric units containing four types of Na^+ ions (Fig. 1c). Specifically, the 6-coordinated Na1 and Na3 as well as the 7-coordinated Na2 and Na4, were bridged by carboxylate and water oxygens to form the 1D Na–O chain along the *c*-axis. After linking the neighboring chains together by L2 linkers, the final IMP-27Na with

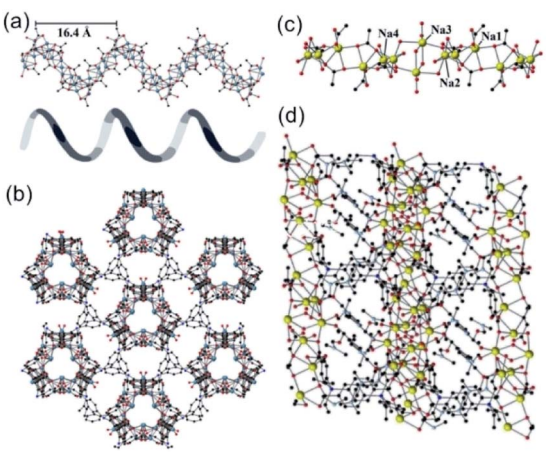

Fig. 1 (a) The 1D helical Li–O chain with a pitch of 16.4 Å observed in IMP-24Li; (b) the projection view of the formed 1D Li–O chain along the [001] direction; (c) the structure presentation of 1D Na–O chain among IMP-27Na; (d) the projection view of the solvent-filled IMP-27Na along the [110] direction. Element color: C is black; O is red; Li is blue; Na is yellow. Reprinted with permission from ref. 42. Copyright 2018, American Chemical Society.

a potential void space of 39% was constructed if the complete removal of all solvents (Fig. 1d).

Moreover, 2D MOFs based on alkali metal have also been reported.[26,43–45] For examples, ULMOF-1 [UL = ultralight, Li_2(2,6-NDC), 2,6-NDC = naphthalene-2,6-dicarboxylate][26] and ULMOF-2 [Li_2(4,4-BPDC), 4,4-BPDC = 4,4-bisphthalboxylate][43] both with lithium ions as metal centers were constructed by using 2,6-NDC and 4,4-BPDC as the organic ligand, respectively. ULMOF-1 was synthesized by heating $LiNO_3$, 2,6-H_2NDC, and ammonia fluoride (NH_4F) as an additive in the mixture of DMF and ethanol at 180 °C. According to the crystallographic data, the structural unit of ULMOF-1 was composed of a novel type of 2D Li–O inorganic sheet bridged by aromatic 2,6-NDC linkers. In which, the lithium center was coordinated with four carboxylate oxygens from 2,6-NDC (Fig. 2a). Subsequently, as-resultant Li–O tetrahedrons in neighboring formed a polyhedral dimer *via* sharing one tetrahedron edge, which was further connected with each other *via* sharing the remaining oxygen corners to extend to be an infinite 2D LiO_2 sheet (Fig. 2c). As building pillars, 2,6-NDC were further spaced at the adjacent LiO_2 layers to construct the final 3D ULMOF-1 skeleton. ULMOF-2 presented an isoreticular structure and was synthesized under other identical reaction conditions except for using 4,4-BPDC as the organic linker (Fig. 2e). Thanks to the larger dimensionality of 4,4-BPDC spaced at adjacent LiO_2 layers, ULMOF-2 (Fig. 2d) exhibited more open channels along the *a*-axis in comparison to ULMOF-1.

The first 2D Na-MOF MOF-705 [Na_4(BDA)(CH_3OH)(H_2O), BDA = (2*S*,2′*S*)-2,2′-(terephthaloylbis(azanediyl))disuccinate] was reported by Yaghi *et al.*[45] MOF-705 was synthesized by heating the methanolic solution involving sodium hydroxide and H_4BDA at 50 °C. The obtained product belonged to the chiral monoclinic $P2_1$ space group and featured a unique 2D sodium oxide layer in infinite extensions along the [100] and [010] directions. Through lengthening the dimensionality of organic ligand, isoreticular MOF-706 [Na_4(BPDA)(CH_3OH)(H_2-O), BPDA = (2*S*,2′*S*)-2,2′-(1,1′-biphenyl)-4,4′(dicarbonyl)bis(azanediyl)disuccinate] could be further obtained.

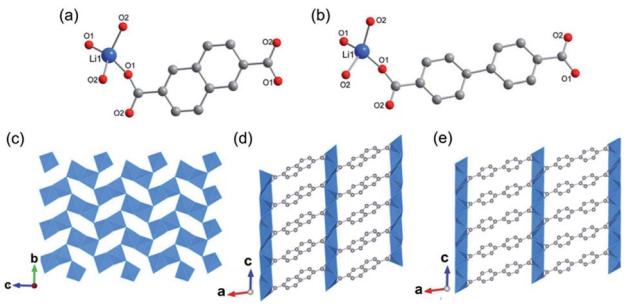

Fig. 2 (a and b) Local coordination environment of the lithium-ion in ULMOF-1 and ULMOF-2, respectively. Reproduced with permission from ref. 26. Copyright 2009, American Chemical Society. (c) An [100] orientation view of the 2D Li–O inorganic sheet. (d and e) The [010] projection view of ULMOF-1 and ULMOF-2, respectively. Element color: C is grey; O is red; Li is blue. Reproduced with permission from ref. 43. Copyright 2009, American Chemical Society.

Apart from the common Li^+- and Na^+-based ISBU MOF examples,[42,46,47] heavier alkaline cations like K^+ and Rb^+ have also been utilized for ISBU MOF constructions.[44] A redox tetracarboxylic acid H_4(TTF-TC) (Fig. 3a) was reported to react with corresponding alkali chloride *via* the hydrothermal method for constructions of 1D K_2H_2(TTF-TC) namely MIL-132(K), and 2D M_2H_2(TTF-TC) (M = K^+ or Rb^+) namely MIL-133(K, Rb). Taking the 1D MIL-132(K) for representation, H_4(TTF-TC), KCl were mixed in the alkaline water containing KOH as the first step. Due to the thermal susceptibility of H_4(TTF-TC), the resultant solution was then heated at a relatively lower reaction temperature (70 °C) to obtain the MIL-132(K) product. According to the resolved crystal structure, there was a novel K–O chain composed of edge-sharing [KO_5] polyhedron found along the [010] direction. Bridged by the carboxylate group in a bidentate fashion, two neighboring single chains are linked together in parallel to form the dimerized K–O chain shown in Fig. 3b. Finally, an open framework belonged to the monoclinic system and a $P2_1/c$ space group was built after TTF-TC linkers being installed within the *a*–*c* plane (Fig. 3d). More interestingly, another novel MIL-133(K) phase characteristic of distinct 2D K–O inorganic sheet structures was obtained *via* simply changing the added amount of KOH (*i.e.* the pH value) in the hydrothermal system. Under other same conditions, MIL-133(K) crystallized in the orthorhombic system and a higher symmetric *Pnmm* group, in which the central K^+ adopted a tetrahedron coordination mode. After being bridged by carboxylate groups in a bidentate fashion, the isolated [KO_4] tetrahedron was compressed into a novel 2D K–O inorganic sheet within the *a*–*b* plane. An isoreticular MIL-133(Rb) with

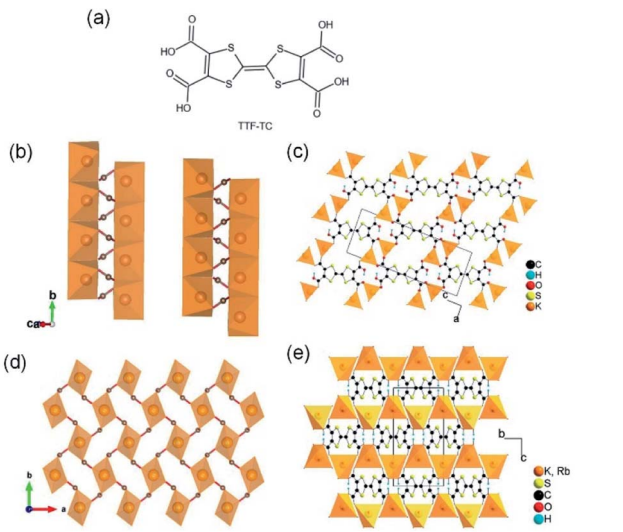

Fig. 3 (a) The chemical structure of tetrathiafulvalene tetracarboxylic acid [H_4(TTF-TC)]; (b) the dimerized 1D K–O inorganic chain among MIL-132(K) which are bundled with carboxylate group; (c) the structure of MIL-132(K) projected view along the [010] direction; (d) the 2D K–O inorganic sheet among the polymorphic MIL-133(K, Rb); (e) the structure of MIL-133(K, Rb) projected view along the [100] direction. Reproduced with permission from ref. 44. Copyright 2010, American Chemical Society.

slightly expanded cell parameters due to the larger radius of Rb^+ could be further obtained by replacing RbCl with KCl simply.

For transition metal(I)-based ISBU MOFs,[48–50] Bai *et al.*[48] reported the $[Cu_6I_6(L3)_3$, L3 = 1,4-bis(phenylthio)but-2-yne] with 1D $[CuI]_n$ ladders by the acetonitrile-based solvothermal synthesis method. According to the resolved single-crystal structure, the Cu(I) cation was coordinated with three μ_3-iodide ions (each was connected with three Cu(I) cations in a bridged way) and hence formed an $[CuI]_n$ ladder along the *a*-axis. In addition, each $[CuI]_n$ ladder was linked to four adjacent ones to construct the final 3D network by sulfur donors on L3.

2.2 ISBU MOFs constituted of metal(II) central ions

Yaghi *et al.*[10] reported a series of 1D Mg-MOFs dating back to 2012. Taking the famed Mg-MOF-74 for representation, the reaction of $Mg(NO_3)_2\cdot 6H_2O$ and H_2L4 (3,3′-dihydroxy-[1,1′-biphenyl]-4,4′-dicarboxylic acid) in the mixed solvent of DMF, H_2O and ethanol at 120 °C produced colorless needle-shaped microcrystals after 24 h. The obtained Mg-MOF-74 crystallized in a trigonal system with the $R\bar{3}$ space group, where Mg^{2+} adopted a 6-coordinated mode with oxygens (three from carboxylate oxygens, two from phenolic hydroxyls and one water oxygen) to form an octahedron (Fig. 4a). These MgO_6 octahedrons were further packed into a triple-helical 1D Mg–O chain with a pitch of 6.8 Å along the crystallographic *c*-axis *via* edge-sharing (Fig. 4b). Finally, a 3D framework with regular honeycomb channels (1.8 nm, Fig. 4c) was constructed after the installation of organic linkers. Noteworthily, half of the chiral Mg–O chains among the whole 3D framework spiraled clockwise while the others spiraled counterclockwise, thereby eventually behaving a racemic character for the overall framework. Interestingly, the chiral Mg-MOF [Mg_2(DOBPTC), $DOBPTC^{4-}$ = 4,4′-di-oxidobiphenyl-3,3′-dicarboxylate] with the same Mg–O chain to Mg-MOF-74 has been further successfully developed by Long.[28] Distinct from the centrosymmetric Mg-MOF-74, as-obtained *R*-Mg_2(DOBPTC) crystallized in a trigonal system with the chiral $P3_221$ space group, in which the triple-helical Mg–O chains followed a clockwise spiral homogeneously. *Vice versa*, the *R*-Mg_2(DOBPTC) crystallized in the chiral $P3_121$ space group and followed a counterclockwise spiral for its Mg–O chains. Moreover, another kind of chiral Mg-MOF structure, which was named as CPF-1, has been synthesized by Feng and his colleagues in 2011.[51] The formula of CPF-1 was [$Mg_2(H_2O)_2$(BPTC), BPTC = 3,3′,5,5′-tetracarboxylate], which was obtained by the hydrothermal reaction of $Mg(NO_3)_2\cdot 6H_2O$ and H_4BPTC in the water and *N*-ethylformamide (NEF) mixed solvent at 120 °C for 72 h. Differently, CPF-1 crystallized in a tetragonal system with the chiral $I4_122$ space group, in which Mg^{2+} was coordinated by four carboxylate oxygens from four BPTC ligands and two water oxygens to form a MgO_6 octahedron (Fig. 4d). Furthermore, these octahedrons were connected along the crystallographic *c*-axis *via* octahedron corner-sharing, which was twisted into a 1D quadruple spiral with a pitch of 12.3 Å (Fig. 4e). After being linked by BPTC likers, as-formed 1D chiral chains were further assembled into a highly opened 3D framework with ordered cylinder channels (1.3 nm, Fig. 4f).

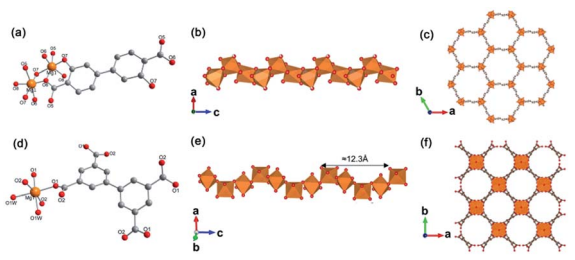

Fig. 4 (a) The coordination environment of Mg(II) ions in Mg-MOF-74; (b) the 1D chain structure of Mg-MOF-74 extending along the *c*-axis; (c) the corresponding 3D framework of Mg-MOF-74 view down the [001] direction. Reproduced with permission from ref. 10. Copyright 2012, AAAS. (d) The coordination environment of Mg(II) ions in CPF-1; (e) the 1D chain structure of CPF-1 extending along the *c*-axis; (f) the corresponding 3D framework of the CPF-1 view down the [001] direction. Reproduced with permission from ref. 51. Copyright 2017, American Chemical Society.

In addition, 1D MOFs based on other alkaline earth metals have been reported.[52–56] For example, Martínez *et al.*[53] synthesized two types of 1D Ca-MOF. The formula of Ca-MOF-1 was [$Ca_3(BTB)_2(DMF)_3$, BTB = 1,3,5-tris(4-carboxyphenyl)benzene], which was obtained by the hydrothermal reaction of $Ca(NO_3)_2\cdot 4H_2O$ and BTB in the water and DMF mixed solvent at 70 °C for 72 h. As obtained Ca-MOF-1 crystallized in a tetragonal crystal system with the chiral space group of *R*3. In which, there were three kinds of coordination modes for Ca^{2+} centers (Fig. 5a). Namely, Ca1 and Ca2 were both coordinated by five carboxylate oxygens from four BTB ligands and one amide oxygen from DMF. While Ca3 was coordinated by six carboxylate oxygens from three BTB ligands and additional one amide oxygen from DMF. Interestingly, the edge-shared octahedral dimer of $Ca1O_6$ and $Ca2O_6$ was further connected to two distorted $Ca3O_7$ pentagonal bipyramids at the two heads by corner oxygen-sharing, eventually forming a robust helical Ca–O chain along the [001] direction by unit repeat (Fig. 5b). Furthermore, the as-formed 1D Ca–O chain was linked with each other by BTB linkers to form the final 3D structure with a porosity of 43% (Fig. 5c). The formula of Ca-MOF-2 was [Ca(BDC)(DMF)(OH_2), BDC = 1,4-benzenedicarboxylate], which was obtained by heating $Ca(NO_3)_2\cdot 4H_2O$ and H_2BDC in the water and DMF mixed solvent at 80 °C for 72 h. The obtained Ca-MOF-2 crystallized in a monoclinic crystal system with the space group of $P2_1/c$. In which, each Ca^{2+} was coordinated by six carboxylate oxygens from two distinct BDC ligands, one water oxygen, and one DMF oxygen. Distinct from Ca-MOF-1, all the Ca centers in Ca-MOF-2 adopted an 8-coordination mode by chelated carboxylate groups. The resultant CaO_8 polyhedrons were further corner-connected with each other to form the 1D Ca–O chain along the [010] direction. Since larger ionic radius, Sr^{2+} (ref. 54 and 57) and Ba^{2+} (ref. 58–60) usually manifested higher coordination numbers among MOFs than the cognate Ca^{2+}. For instance, Wang *et al.*[57] synthesized a 1D Sr-MOF-1 [Sr(BDC)(H_2O)(DMF)] by the reaction of $Sr(NO_3)_2$ and H_2BDC in the H_2O and DMF mixture at 100 °C for three days. The obtained Sr-MOF-1 crystallized in a monoclinic system with the $P2_1/c$ space group, where the Sr^{2+} exhibited an 8-coordinated

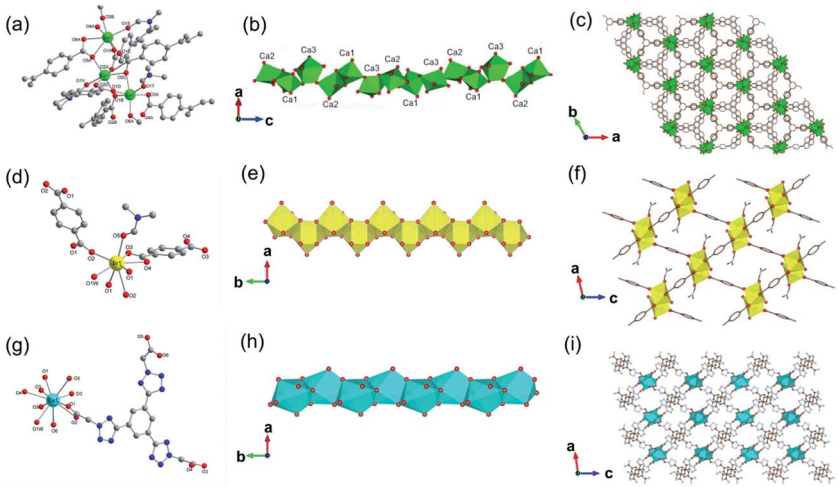

Fig. 5 (a) The coordination environment of Ca(II) ions in Ca-MOF-1; (b) the 1D chain structure of Ca-MOF-1 projected along the *b*-axis; (c) corresponding 3D skeleton structure of Ca-MOF-1 projected along the *c*-axis. Reproduced with permission from ref. 53. Copyright 2018, Royal Society of Chemistry. (d) The coordination environment of Sr(II) ion in Sr-MOF-1; (e) the 1D chain structure formed by Sr(II) ions; (f) the corresponding 3D porous framework of Sr-MOF-1 after removal of coordinated solvent molecules. Reproduced with permission from ref. 57. Copyright 2021, WILEY-VCH Verlag GmbH. (g) The coordination environment of Ba(II) ion in Ba-MOF-1; (h) the 1D infinite $[Ba(-CO_2)_3Ba]$ chain projected along the *c*-axis; (i) the anionic 3D framework ($[Ba(L5)(H_2O)]^-$) of Ba-MOF-1. Reproduced with permission from ref. 58. Copyright 2021, Royal Society of Chemistry.

environment with six carboxylate oxygens from four BDC ligands, one DMF molecule oxygen and one water molecule oxygen (Fig. 5d). In this MOF, the SrO_8 polyhedrons were bridged by carboxylate groups to form a 1D chain along the crystallographic *b*-direction, which were further linked by BDC linkers to form a 3D framework with rhombic open channels (Fig. 5e and f). What's more, Zhu *et al.*[58] recently constructed a 1D Ba-MOF-1 *via* reacting $BaCl_2 \cdot 2H_2O$ and 1,3,5-tri(2-carboxymethyltetrazol-5-yl)benzene (L5) in the water and DMF mixture at 120 °C. As-obtained Ba-MOF-1 with the formula of $[Me_2NH_2][Ba(L5)(H_2O)]$ crystallized in a monoclinical crystallographic system and a *C*2/*c* space group. In which, each Ba^{2+} was coordinated by nine carboxylate oxygens from six distinct ligands and one water oxygen. Meanwhile, each carboxylate group from L5 chelated to two Ba^{2+} *via* a tridentate coordination mode (Fig. 5g). As shown in Fig. 5h, the resultant BaO_{10} spheno corona polyhedrons were further packed into a 1D infinite $[Ba(-CO_2)_3Ba]$ chain along the *b*-axis *via* sharing three bridging carboxylates (namely sharing one face of the polyhedron). Finally, each 1D chain was linked to four adjacent chains nearby within the *a*–*c* plane by four L5 linkers for the construction of a negative-charged 3D network ($[Ba(L4)(H_2O)]^-$). To balance the charge, additional $[Me_2NH_2]^+$ ions produced from the *in situ* decomposition of DMF were trapped into channels (7 Å) of the network to form the 3D $[Me_2NH_2]$ $[Ba(L4)(H_2O)]$ framework (Fig. 5i). Topologically, the L5 linker was derived as the 3-connected node simply. Meanwhile, the $[Ba(-CO_2)_3Ba]$ could be simplified to the 1D face-sharing octahedron chain *via* connecting two types of 7-connected carboxylate C atoms. Hence, a trinodal 3,7,7-connected net with the Schläfli symbol $(3^7 \cdot 4^6 \cdot 5^2 \cdot 6^2 \cdot 7^4)(3^7 \cdot 4^6 \cdot 5^2 \cdot 6^3 \cdot 7^3)_2(6^3)$ could be assigned to the resultant 1D Ba-MOF-1. Martínez *et al.*[53] synthesized another type of 1D Ba-MOF-2 in 2018 using $Ba(NO_3)_2$ and 2-amino-1,4-benzenedicarboxylic acid (NH_2–H_2BDC) in a water–DMF mixed solvent at 80 °C for 72 h. It was formulated as [Ba(NH_2–BDC)(DMF)] and crystallized in a trigonal crystallographic system with the chiral $P3_1$ space group for Ba-MOF-2. The Ba^{2+} was an 8-atom coordination mode by seven oxygen atoms from five distinct NH_2–BDC linkers and one DMF oxygen. In detail, Ba^{2+} were connected by NH_2–BDC in the tridentate and bidentate bridging way to form a spiral 1D Ba–O chain along the crystallographic *c*-axis *via* edge-sharing.

Up to now, there are a few reports of alkaline earth metal (Ca, Sr and Ba)-based 2D MOFs.[61–68] In 2008, Loiseau *et al.*[66] synthesized a 2D Ca-MOF-3 named [$Ca_2(OH)_2$(NDC), NDC = 2,6-naphathalenedicarboxylate] by reacting $Ca(OH)_2$ and H_2NDC in the dilute HNO_3 solution at 180 °C for 24 h. The obtained Ca-MOF-3 crystallized in the monoclinic and $P2_1/c$ space group. Each Ca^{2+} was the 7-atom coordination with four carboxylate oxygen atoms from four NDC ligands and three hydroxyl groups (Fig. 6a). In detail, the carboxylate oxygens (O1 and O3) of NDC adopted the μ_3-bridging fashion with two Ca^{2+} and one C, as same as the μ_3-hydroxyl group (O2) but with three Ca^{2+} ions. After edge-sharing each CaO_7 mono-capped trigonal prism, a 2D lamellar $Ca_2(OH)_2$ structure was formed within the *b*–*c* plane (Fig. 6b), which was further pillared by NDC linkers along the *a*-direction to form the 3D framework (Fig. 6c). Chen *et al.*[67] synthesized a 2D Sr-MOF formulated as $[Me_2NH_2]_2[Sr_5(BTC)_4(H_2O)_5]$ (BTC = 1,3,5-benzenetricarboxylate) by using $Sr(NO_3)_2$ and H_3BTC in the DMF-water mixed solution. The Sr-MOF-2 crystallized in the orthorhombic system and the space group of $C222_1$, in which Sr^{2+} behaved three distinct coordination modes. That was, Sr1 was coordinated by seven carboxylic oxygen atoms from five distinct BTC linkers and one water oxygen, and Sr2 was also coordinated by seven carboxylate oxygen atoms from six distinct BTC linkers and one water

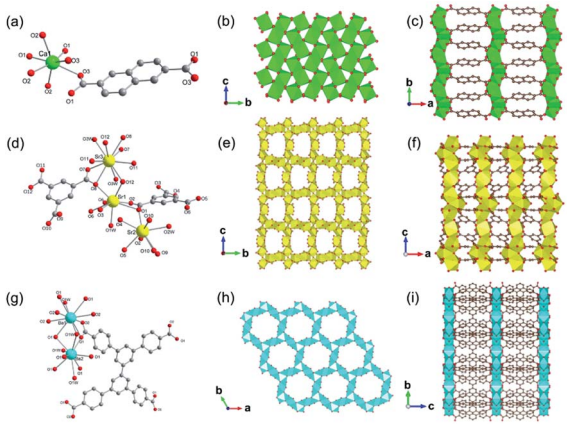

Fig. 6 (a) The coordination environment of Ca(II) ion in Ca-MOF-3. O2 were oxygen atoms from the hydroxyl groups; (b) the 2D lamellar structure of the formed Ca–O sheet; (c) the 3D structure of Ca-MOF-3 projected along the *c*-axis. Reproduced with permission from ref. 66. Copyright 2008, American Chemical Society. (d) The coordination environment of Sr(II) ions in Sr-MOF-2; (e) the 2D inorganic Sr–O layer of Sr-MOF-2; (f) the 3D cylindrical framework of Sr-MOF-2 view down the *b*-axis. Reproduced with permission from ref. 67. Copyright 2013, Elsevier Inc. (g) The coordination environment of Ba(II) ions in Ba-MOF-3; (h) the 2D inorganic Ba–O–Ba layer view down the *c*-axis; (i) the 3D open structure of formed Ba-MOF-3 view down the *a*-axis. Reproduced with permission from ref. 68. Copyright 2014, Royal Society of Chemistry.

oxygen. Moreover, Sr3 was 10-coordinated by eight carboxylate oxygen atoms from four distinct BTC linkers and two water oxygens (Fig. 6d). A crown-like tetranuclear cluster [Sr_4(-COO)$_6$(O1w)] was formed by two symmetrically related $Sr1O_8$ and $Sr2O_8$ pairs, which were connected with each other *via* the μ_2-oxygens to form a 1D chain. As-formed 1D SrO chains were further bridged by the $Sr3O_{10}$ polyhedrons to construct a 2D inorganic Sr–O layer (Fig. 6e). Finally, a unique 3D pillar-layered structure was built after linking those 2D Sr–O layers by BTC linkers (Fig. 6f).

Feng *et al.*[68] reported a 2D Ba-MOF-3 with the formula of [$Me_2NH_2^+$]$_2$ [Ba_5(L6)$_3$(H_2O)$_6$] (L6 = 3,3′,5,5′-biphentetrolate) by using $Ba(NO_3)_2$ and H_4L6 in the DMF-water mixed solution at 140 °C for 48 h. The Ba-MOF-3 crystallized in the tetragonal system and the *P*6/*m* space group. In this framework, Ba^{2+} had two coordination modes including the 10-coordinated Ba1 with four chelated carboxylate groups from four distinct ligands and two coordinated water oxygens, and the 9-coordinated Ba2 with six monodentate carboxylate oxygen atoms from six distinct ligands and three terminal water oxygens (Fig. 6g). Interestingly, each $Ba1O_{10}$ polyhedron was connected to two $Ba2O_9$ polyhedrons, and meanwhile, each $Ba2O_9$ polyhedron was connected to three neighboring $Ba1O_{10}$ polyhedrons *via* face-sharing, forming a 2D honeycomb Ba–O inorganic layer (Fig. 6h) consequently. Furthermore, these lamellar structures were connected by the tetratopic ligands along the crystallographic *c*-axis to form the final 3D framework with the charge neutralization of $Me_2NH_2^+$ (Fig. 6i).

One can easily find that there are more examples of alkali earth metal-based ISBU MOFs thanks to their higher coordination numbers and stronger coordination strength in comparison to the group I metals. Even more, unique and rare MOF examples characteristic of the corresponding 3D metal-oxo net were also reported.[24,69–72] For example, Henderson and his colleagues[71] synthesized a type of 3D Mg-MOF-1 [$Mg_3(O_2CH)_6$] by using $Mg(NO_3)_2 \cdot H_2O$ and formic acid in DMF at 110 °C for 40 h. The Mg-MOF-1 product crystallized in the monoclinic crystallographic system and the $P2_1/c$ space group, in which Mg^{2+} had four kinds of coordination environments. Namely, Mg1 was coordinated by six μ_2-O, both Mg2 and Mg4 were coordinated by four monodentate oxygens and two μ_2-O, while Mg3 was coordinated by two monodentate oxygens and four μ_2-O, noting that all oxygen atoms came from formates (Fig. 7a). Then, the formed $Mg3O_6$ was connected to $Mg1O_6$ by edge-sharing, while $Mg2O_6$ and $Mg4O_6$ were both connected to $Mg1O_6$ by corner-sharing, thus forming a complex 3D Mg–O inorganic net (Fig. 7b and c) with exposing open 1D channels view down the *b*-axis (Fig. 7b). Ok *et al.*[72] synthesized a type of 3D Sr-MOF named CAUMOF-8 [Sr_2(BTC)(NO_3)] by using $Sr(NO_3)_2$, $N(CH_3)_4Cl$, and H_3BTC in the HNO_3 and DMF mixture at 180 °C for 72 h. The CAUMOF-8 crystallized in the hexagonal crystallographic system and the $P\bar{6}2c$ space group. In which, two types of Sr^{2+} with different coordination modes were observed according to the single-crystal diffraction characterization. In detail, Sr1 was a 9-coordination and formed a $Sr1O_9$ polyhedron, while Sr2 was an 8-coordination and formed a $Sr2O_8$ polyhedron (Fig. 7d). Within the *a*–*b* plane, there were three $Sr2O_8$ polyhedrons packed together to form a trimer *via* edge-sharing, which was further bridged by face-shared $Sr1O_9$ polyhedrons to construct an infinite Sr–O inorganic sheet with exposure of 1D open channels (Fig. 7e). Along the *c*-axis, as $Sr1O_9$ polyhedrons were further connected with each other *via* edge-sharing, a unique 3D Sr–O inorganic net was obtained (Fig. 7f). Thanks to the pure inorganic skeleton, CAUMOF-8 has exhibited excellent thermal stability up to 520 °C according to the thermogravimetric analysis (TGA) result.

The first 3D Ba-MOF-4 structure was reported by Yao and his colleagues,[70] who carried out the synthesis by dissolving $Ba(NO_3)_2$ and H_3BTC in the mixed water and DMF solution at room temperature for 30 minutes, and then reacted at 110 °C for 4 days. The Ba-MOF-4 product with the molecular formula of [Ba_3(BTC)$_2$(H_2O)$_4$] crystallized in the orthorhombic crystal system and $Pna2_1$ space group. In a cell unit, there were three types of crystallographic independent Ba(II) ions (Ba1, Ba2 and Ba3), two BTC linkers and four coordinated water molecules. Ba1 was coordinated to four carboxylate oxygens from four independent BTC ligands and three hydroxyl oxygens, forming a slightly distorted $Ba1O_7$ triangular prism. Ba2 was eight-coordinated with seven oxygen atoms from seven different BTC linkers and one terminal water oxygen, forming a $Ba2O_8$ square anti-prismatic structure. While Ba3 was nine-coordinated by eight carboxylate oxygens from five different BTC linkers and one terminal water ligand, thereby adopting a $Ba3O_9$ single-capped square anti-prismatic geometry (Fig. 7g). Furthermore, each $Ba1O_7$ polyhedron was linked to one $Ba2O_8$ and one $Ba3O_9$ *via* edge-sharing, and to another $Ba3O_9$ *via* corner-sharing. At the same time, the $Ba2O_8$ polyhedron was

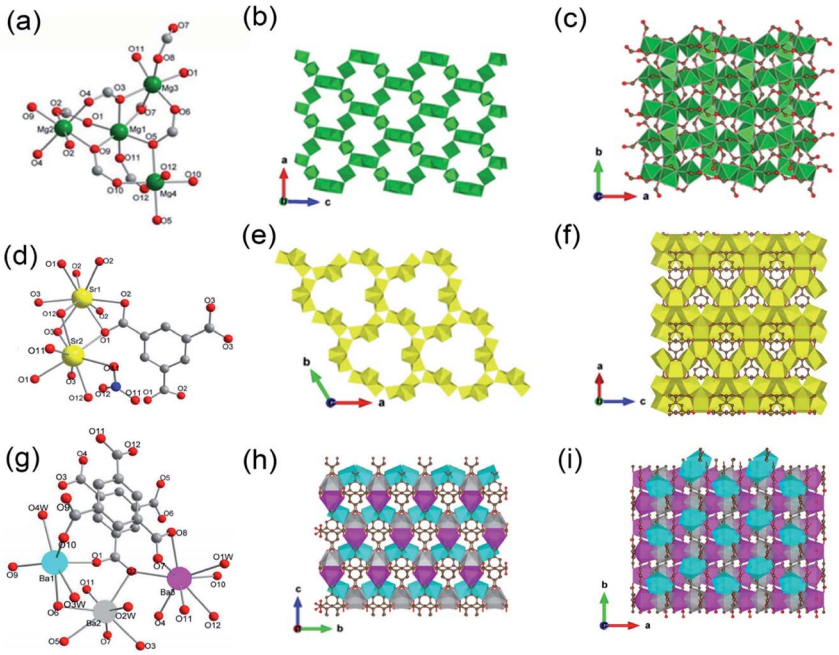

Fig. 7 (a) The coordination pattern diagram of the Mg center among Mg-MOF-1; (b) A 2D surface map formed among the Mg-MOF-1 projected along the *b*-direction; (c) the local view of the Mg-MOF-1 projected along the *c*-direction. Reproduced with permission from ref. 71. Copyright 2006, American Chemical Society. (d) The coordination pattern diagram of the Sr center among CAUMOF-8; (e) a 2D surface map formed by the CAUMOF-8 projected along the *c*-direction; (f) the local view of the CAUMOF-8 projected along the *b*-direction. Reproduced with permission from ref. 72. Copyright 2011, American Chemical Society. (g) The coordination pattern diagram of the Ba center among Ba-MOF-4; (h) a 2D surface map formed by Ba-MOF-4 projected along the *a*-direction; (i) the local view of the Ba-MOF-4 projected along the *c*-direction. Reproduced with permission from ref. 70. Copyright 2012, American Chemical Society.

linked to one corner-shared $Ba3O_9$ additionally (Fig. 7h). As a result, the accumulation of these polyhedrons formed a unique 3D inorganic Ba–O framework finally (Fig. 7i).

Transition metals have additional d-orbitals available for bonding with linkers, therefore transition metal-based ISBU MOFs exerted better stability normally and have been widely studied.[73–79] He and his colleagues[76] synthesized a series of 1D Fe(II)-MOF characteristic of excellent thermal stability. Taking the Fe(II)-MOF-1 [$Fe(6\text{-}H_2MNA)_2$, 6-H_2MNA = 6-mercaptonicotinic acid] for representation, it was produced by the reaction of [$CpFe(CO)_2$, Cp = cyclopentadienyl] and 6-H_2MNA at 160 °C for 2 days in a mixed solvent of toluene and water. $Fe(6\text{-}H_2MNA)_2$ crystallized in a monoclinic system with the $P2_1/c$ space group, wherein Fe^{2+} was 6-atom coordinated by four S atoms and two carboxylate oxygens from two different 6-H_2MNA linkers, thereby forming a FeS_4O_2 octahedron (Fig. 8a). After bridging by μ_2-S atoms, the polyhedron was packed into an infinite $[FeO_2S_2]_n$ chain along the *a*-axis, which was further connected with four neighboring ones by the 6-H_2MNA linker to form the final 3D framework (Fig. 8b and c). Ji *et al.*[79] used 1,4-bis(2-methylbenzimidazol-1-methylmethyl)benzene (BMB), H_4BPTC and $Cd(NO_3)_2\cdot 4H_2O$ to obtain a 1D Cd-MOF-1 [$Cd_2(BMB)_{0.5}$(-BPTC)] in water at 160 °C for 4 days. The obtained Cd-MOF-1 crystallized in the triclinic system and the $P\bar{1}$ space group, in which Cd^{2+} had two types of coordination modes. Namely, Cd1 was coordinated by seven carboxylate oxygens from five different BPTC linkers and Cd2 was coordinated by five carboxylate oxygens from four different BPTC and one N atom from the BMB (Fig. 8d). Two edge-sharing $Cd1O_7$ polyhedrons and two edge-sharing Cd_2O_5N polyhedrons were joined as the

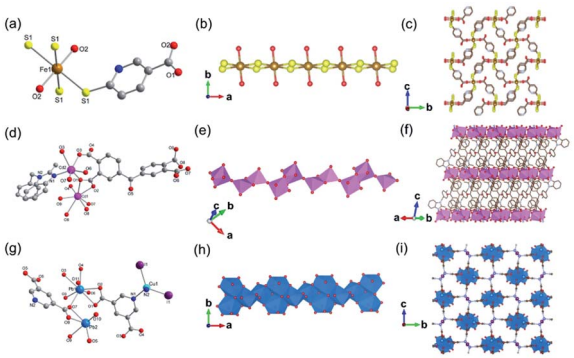

Fig. 8 (a) The coordination mode of Fe(II) ion among the Fe(II)-MOF-1; (b) the 1D chain structure of $[FeO_2S_2]_n$; (c) the 3D framework structure of Fe(II)-MOF-1 projected along the *a*-axis. Reproduced with permission from ref. 76. Copyright 2021, American Chemical Society. (d) The coordination modes of Cd(II) ions among Cd-MOF-1; (e) the 1D chain structure of Cd-MOF-1; (f) the 3D framework structure of Cd-MOF-1 projected along the *a*-axis. Reproduced with permission from ref. 79. Copyright 2017, Elsevier Inc. (g) The coordination modes of Pb(II) and Cu(I) among the 1D PbCu-MOF-1; (h) An infinite 1D chain formed by the connection of Pb(II)-oxo polyhedrons; (i) the 3D framework structure of PbCu-MOF-1 view down the [100] direction. Reproduced with permission from ref. 75. Copyright 2021, American Chemical Society.

repeat unit by corner-sharing, which additionally shared head and tail corners to form the corresponding 1D chain (Fig. 8e). Finally, those 1D chains were connected by BPTC linkers to construct a 3D framework (Fig. 8f). Moreover, Pan *et al.*[75] reported a novel 1D heterometallic MOF [$Pb_4Cu_2I_2(PDC)_4(DMF)_6$, PDC = 3,5-pyridinedicarboxylate] recently, which was synthesized by mixing CuI, PbI_2, and H_2PDC in the DMF solution at room temperature for 4 days. According to the single-crystal X-ray characterization, the obtained PbCu-MOF-1 crystallized in the monoclinic system and the $P2_1/c$ space group. In detail, there were two kinds of Pb coordinations in the repeated unit. That was, the 8-coordinated Pb1 by oxygens from 5 distinct PDC linkers and one DMF molecule, and the 5-connected Pb2 by three bridging carboxylate oxygens and two DMF oxygens (Fig. 8g). Correspondingly, the formed $Pb1O_8$ polyhedron and $Pb2O_5$ bipyramid were bridged by shared carboxylate groups from PDC, resulting in the 1D infinite Pb–O chain along the [100] direction (Fig. 8h). Furthermore, discrete Cu_2I_2 SBU as additional joint sites *via* binding to the pyridyl nitrogens of PDC, linked four adjacent 1D chains to construct the final 3D framework (Fig. 8i). Guo *et al.*[80] synthesized a novel 2D PbAg-MOF-1 [$AgPb(BTC)(H_2O)$] by the hydrothermal reaction of $Pb(OAc)_2\cdot 3H_2O$, $AgNO_3$, H_3BTC and NaOH in water at 170 °C for 3 d. As-obtained PbAg-MOF-1 crystallized in a triclinic crystal system with the space group of $P\bar{1}$. According to the well-resolved crystallographic structure, each Ag^+ was a 5-atom coordination fashion with four carboxylate oxygens from four inequivalent BTB linkers and one water oxygen. While, each Pb^{2+} was a 7-atom coordination fashion with seven carboxylate oxygens from five inequivalent BTB linkers to form a PbO_7 polyhedron. Interestingly, the 1D Ag–O chain formed *via* edge-shared AgO_5 polyhedrons and the 1D Pb–O chain connected *via* edge-shared PbO_7 polyhedrons were parsed in the cell. Moreover, those chains were connected with each other *via* SBUs corner-sharing to form a condensed 2D Ag–O–Pb plate within the *a*–*c* plane. Finally, the 2D structure was further linked by BTC to form the final 3D framework.

With concerns on 3D examples,[22,23] Lin *et al.*[23] constructed a 3D [$Cd_3Na_6(BTC)_4(H_2O)_{12}$] *via* reacting $Cd(CH_3COO)_2\cdot 2H_2O$, H_3BTC and NaOH in the water–dimethylacetamide mixture at 130 °C for 5 days. The obtained CdNa-MOF-1 crystallized in the tetragonal system and the $P4_2/n$ space group. In one unit, Cd^{2+} had two kinds of coordination modes. Namely, Cd1 was coordinated by six carboxylate oxygens from four distinct BTC linkers to form a distorted octahedron, and Cd2 was rarely coordinated by eight carboxylate oxygens from four distinct BTC linkers to form a polyhedron of $Cd2O_8$. Thanks to the bridging of BTC linkers, a 3D single $Cd_3(BTC)_4$ framework whose building unit was composed of two $Cd1O_6$ octahedrons, one $Cd2O_8$ polyhedron and four BTC linkers was formed. Interestingly, the potential cavities of a single $[Cd_3(BTC)_4]_n$ framework were interpenetrated with another set of identical framework for energy minimization in thermodynamics. As the secondary metallic central, Na^+ had two kinds of coordination modes. That was, Na1 was coordinated by four carboxylate oxygens from four distinct BTC linkers and two μ_2-H_2O oxygens to form a distorted octahedron, and Na2 was coordinated by four oxygens from four μ_2-H_2O and two terminal water oxygens to form a distorted octahedron (Fig. 9a). Those polyhedrons including two $Na1O_6$ and one $Na2O_6$ formed a $Na3O_{12}$ trimer *via* face-sharing, which further acted as the bridge across the two sets of interpenetrated $[Cd_3(BTC)_4]_n$ frameworks to construct the final 3D MOF (Fig. 9b and c).

In 2019, there was a type of 3D Pb(II) MOF (KGF-1) reported by Tanaka *et al.*[22] KGF-1 with the empirical formula of $Pb_3TTC_2\cdot 2H_2O$ (TTC = trithiocyanuric acid) was obtained by reacting $Pb(NO_3)_2$ and TTC in the mixed DMSO and water solution at 100 °C for 24 h. In this framework, there were two coordination

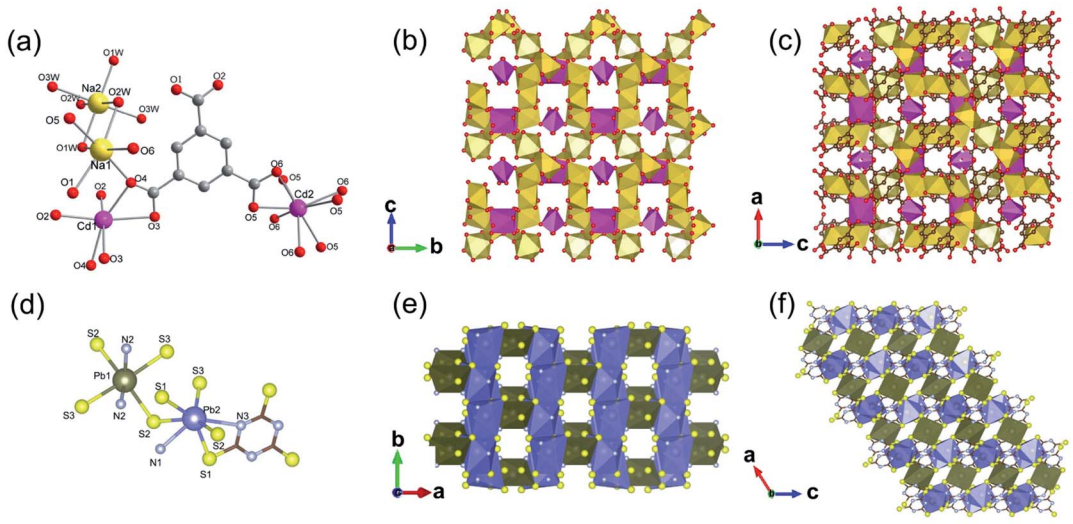

Fig. 9 (a) The coordination environment of Cd(II) ions and Na(I) ions among the 3D CdNa-MOF-1; (b and c) the polyhedral structure diagram of CdNa-MOF-1 within the *b*–*c* plane and *a*–*b* plane, respectively. Reproduced with permission from ref. 23. Copyright 2011, American Chemical Society. (d) The coordination environment of Pb(II) ions among KGF-1; (e and f) the polyhedral structure diagram of KGF-1 within the *a*–*b* plane and *a*–*c* plane. Reproduced with permission from ref. 22. Copyright 2019, American Chemical Society.

environments for central Pb^{2+}, which gave rise to corresponding $Pb1S_4N_2$ and $Pb2S_5N_2$ polyhedrons as shown in Fig. 9d. Accordingly, a 1D chain-like SBU extended infinitely along the *b*-axis *via* edge-shared packing of $Pb2S_5N_2$ polyhedrons (Fig. 9e). As the joint, the 0D $Pb1S_4N_2$ polyhedron was connected to four neighboring 1D chains *via* corner-sharing, as illustrated by the 2D projection view of the constructed framework along the *b*-axis (Fig. 9f).

2.3 ISBU MOFs constituted of metal(III) central ions

1D Al-MOFs have been substantially found and investigated thanks to their unique breathing dynamics, outstanding stabilities and abundant resource on the earth.[3,81–88] For example, Yaghi *et al.*[3] synthesized the 1D Al-MOF through the reaction of $AlCl_3$ and 1*H*-pyrazole-3,5-dicarboxylic acid (H_2PZDC) in an alkaline aqueous solvent at 100 °C. The obtained MOF-303 with the molecular formula [Al(OH)(PZDC)] belonged to the monoclinic crystal system and $P2_1/c$ space group. Among it, Al^{3+} centers were all coordinated by four carboxylate oxygens from four different ligands and two hydroxyl ions (Fig. 10a). The resulting AlO_6 octahedrons were arranged into 1D infinite helical [Al(–OH)Al] chains by sharing polyhedron corners along the *a*-axis (Fig. 10b). Moreover, adjacent [Al(–OH)Al] chains were linked by PZDC linkers to construct the open 3D network with a **xhh** topology (Fig. 10c). By simply replacing H_2PZDC with the H_2FDC (furan-2,4-dicarboxylic acid), isoreticular MOF-333 [Al(OH)(FDC)] with nearly identical crystallographic structures was obtained as well. Reinsch and his colleagues[86] constructed another 1D Al-MOF example by allowing $Al_2(SO_4)_3 \cdot 18H_2O$ and citraconic acid to react in an alkaline aqueous solution at 100 °C. The produced CAU-15-Cit with the molecular formula of $[Al_2(OH)_4(O_2C–C_3H_4–CO_2)]$ was ascribed to the monoclinic system and the *C*2/*c* space group. Among CAU-15-Cit, each Al^{3+} was coordinated by four oxygen atoms from hydroxyl ions and two carboxylate oxygens coming from two different citraconates (Fig. 10d). Similarly, the resultant AlO_6 octahedrons were packed into 4-fold helical Al–O chains along the *c*-axis by sharing polyhedron edges (Fig. 10e). Moreover, adjacent chains were interconnected by citraconate linkers together to form 2D infinite layers which were further stacked in an *AAA* fashion to build the 3D framework finally (Fig. 10f). Such 1D Al–O ISBU has also been observed elsewhere[88] and not described duplicately herein.

One more example of Al-MOFs needs to be mentioned, which was synthesized by the reaction between 4,4′-oxydibenzoic acid (H_2OBD) with $Al(NO_3)_3 \cdot 9H_2O$ in a water–DMF mixture at 120 °C.[84] The produced 1D CAU-8-OBD with the formula of $[Al(HODB)_2(OH)]$ crystallized in the tetragonal crystal system and the $I4_1/a$ space group. Specifically, each Al^{3+} was coordinated by four carboxylate oxygens and two aqueous oxygens (Fig. 10g). Unusually, the resulting AlO_6 octahedrons formed two types of 1D Al–O chains by corner-sharing that extended independently along the *a*- and *b*-axis, respectively (Fig. 10h). Furthermore, those mutually perpendicular chains were connected with each other by the V-shaped ODB linkers, thus constructing a 3D framework with spherical cavities of a diameter of 6.4 Å (Fig. 10i).

Among the group III elements, Ga^{3+} (ref. 89–91) and In^{3+}(ref. 92–94) are rarely reported as corresponding ISBU MOFs. Regarding In-MOF, Reinsch *et al.*[93] obtained 1D CAU-43 In(OH)$[Fe(C_5H_4)_2(COO)_2]$ *via* using the conventional solvothermal method. In detail, CAU-43 was synthesized by the reaction of $InCl_3$ and 1,1′-ferrocenedicarboxlic acid (H_2FcDC) in a water–DMF mixture at 80 °C. As-produced CAU-43 crystallized in the monoclinic crystal system and the *C*2/*c* space group. In which, In^{3+} also adopted a 6-connected mode with five carboxylate oxygen atoms from FcDC and the remaining one from water (Fig. 11a). The resulting InO_6 octahedra were further packed into 1D quadruple chiral helical In–O chains along the *c*-axis *via* shared corners (Fig. 11b), which were further connected by FcDC linkers to construct a 3D framework with tetragonal channels (Fig. 11c). In addition to CAU-43, another MOF product with similar 1D In–O inorganic chains was designed and synthesized by changing the metal source to $In(NO_3)_3$ and reaction solvent to the water/methanol/acetic acid-based ternary mixture. As-produced In-MIL-53-FcDC_a with the molecular formula of In(OH)$[Fe(C_5H_4)_2(COO)_2]$ crystallized in the same space group and also adopted the 6-coordination for central In^{3+}. However, InO_6 octahedrons were found packed into a straight achiral In–O chain *via* the co-occupation of para-corners. Furthermore, adjacent chains were connected by FcDC linkers to assemble a 3D framework with narrower pores than CAU-43. As a rare example, Stock and his colleagues[91] report a 1D Ga-MOF [Ga(OH)(TDC), CAU-51] synthesized from $Ga(NO_3)_3$ and 2,5-thiophenedicarboxylic acid (H_2TDC) in an acetic acid and water (v/v, 5/1) mixture at 120 °C. CAU-51 was assigned to the monoclinic crystal system and the $P2_1/c$ space

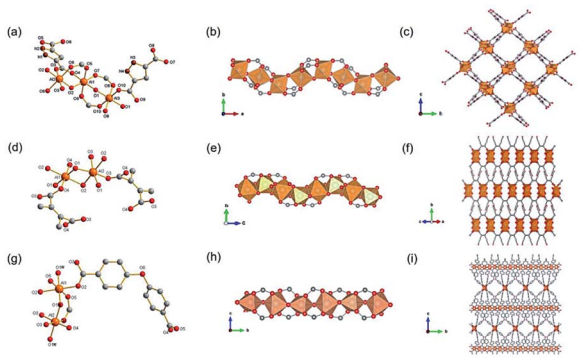

Fig. 10 (a) The coordination environment of Al(III) ions among MOF-303. O1, O2 were both oxygen atoms from the hydroxyl groups; (b) the 1D infinite [Al(–OH)Al] chain extending along the *a*-axis; (c) the 3D framework structure of MOF-303. Reproduced with permission from ref. 3. Copyright 2021, AAAS. (d) The coordination environment of Al(III) ions among CAU-15. O1, O2 were both oxygen atoms from the hydroxyl groups; (e) the 1D chain structure condensed by AlO_6 octahedrons; (f) the 3D porous framework of CAU-15. Reproduced with permission from ref. 86. Copyright 2018, Royal Society of Chemistry. (g) The coordination environment of Al(III) ions among CAU-8-OBD; (h) the 1D chain structure pattern of CAU-8-OBD running along the *b*-axis; (i) the 3D framework of CAU-8-OBD. Reproduced with permission from ref. 84. Copyright 2017, American Chemical Society.

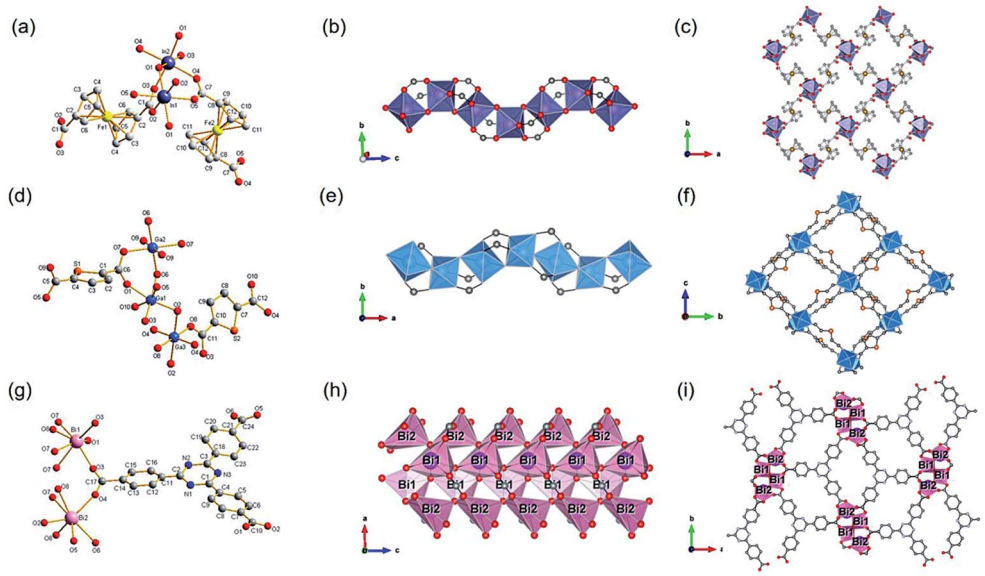

Fig. 11 (a) The coordination environment of In(III) ions among CAU-43; (b) the 1D infinite InO_6 octahedral chain running along the *c*-axis; (c) the 3D framework structure of CAU-43 vie down the *c*-axis. Reproduced with permission from ref. 93. Copyright 2020, American Chemical Society. (d) The coordination environment of Ga(III) ions among Ga-CAU-51. O2, O6 were both hydroxyl oxygen atoms; (e) the 1D chain structure of Ga–O running along the *a*-axis; (f) the 3D porous framework of CAU-51 projected at the *a*-axis. Reproduced with permission from ref. 91. Copyright 2021, American Chemical Society. (g) The coordination environment of Bi(III) ions among CAU-35. O7 was from μ_4-O^{2-} ions and O8 was from μ_3-OH^- ions; (h) the 1D chain ISBU pattern of CAU-35; (i) the projected view of 3D framework of CAU-35 along the *c*-axis. Reproduced with permission from ref. 96. Copyright 2017, Royal Society of Chemistry.

group, where Ga^{3+} was coordinated by four carboxylate oxygens from four different linkers and two oxygens from water (Fig. 11d). The resulting GaO_6 octahedra formed a 1D quadruple chiral helical chain extending infinitely along the *a*-axis by sharing the edges of the octahedra (Fig. 11e). These chains were further interconnected by TDC linkers and formed square 1D channels with a diameter of about 6.2 Å along the [100] direction (Fig. 11f). Note that, this structure was isoreticular to the previously described MOF-303 in fact. Bi(III) normally exhibits similar coordination fashions[89,95,96] to group III elements and therefore was introduced herein by exemplifying one Bi-MOF example. Stock *et al.*[96] used $Bi(NO_3)_3 \cdot 5H_2O$ and 1,3,5-triazine-2,4,6-tribenzoate (TATB) in the DMF/CH_3OH mixed solution to construct corresponding Bi-MOF [$Bi_2(O)(OH)(TATB)$, CAU-35] which crystallized in the orthorhombic crystal system and the $Pna2_1$ space group. Among it, Bi^{3+} were all 7-coordinated but with two different coordination environments. Specifically, Bi1 was linked to three carboxylate oxygens of three different ligands, three μ_4-oxo ions and one μ_3-OH^-. While Bi2 was also linked to four carboxylate oxygens of three different ligands but one μ_4-oxo ion and two μ_3-OH^- ions (Fig. 11g). Interestingly, the $Bi1O_7$ polyhedrons were interconnected into a chain by sharing edges, while the $Bi2O_7$ polyhedron also formed a 1D chain but by sharing corners. Moreover, both two Bi1O and Bi2O chains were bundled to give a 1D chain tetramer *via* sharing corners (Fig. 11h). After the connection of tridentate TATB linkers, the final 3D framework was built with rhombic 1D channels view down the *c*-axis (Fig. 11i).

Besides, ISBU MOFs based on transition metals(III) have also been prevailingly studied.[21,31,97–100] The recently emerged CAU-50 (ref. 99) [$Sc_2(FcDC)_3$] was a 1D Sc-MOF constructed by reacting $Sc(NO_3)_3 \cdot 5H_2O$ with H_2FcDC in a mixture of water and DMF at 95 °C. CAU-50 crystallized in the orthorhombic crystal system and the *Pnna* space group, where the Sc^{3+} center was attached by six carboxylate oxygens from different linkers (Fig. 12a). An infinite ScO_6 octahedral chain along the *a*-axis was formed by the μ_2-bridged carboxylate group (Fig. 12b). Because of the rotatable conformation of FcDC linker, each chain was connected to four adjacent chains *via* FcDC linkers of the antiperiplanar (177.1°, a torsion angle between two carboxylate groups on FcDC) and the anticlinical (136.1°) conformations, thus constructing a 3D framework with relatively narrow cavities (Fig. 12c). What's more, FcDC linkers of the synclinical conformations (44.2°) were also observed as the capping modulator attached to the 1D chain. Recently, Schröder *et al.*[31] constructed a 1D Cr-MOF [$Cr_2(OH)_2(L7)$, denoted as MFM-300(Cr)] by the reaction of $CrCl_3 \cdot 6H_2O$ and biphenyl-3,3′,5,5′-tetracarboxylic acid (H_4L7) in dilute chloride acid aqueous solution. Among MFM-300(Cr), each Cr^{3+} was also 6-coordinated by four carboxylate oxygens and two hydroxyl oxygens (Fig. 12d). The formed $CrO_4(OH)_2$ octahedron further extended its dimension along the *c*-axis to form a 1D polyhedral chain bridged by carboxylate and μ_2-OH groups (Fig. 12e). Finally, adjacent 1D chains were connected by L7 among them to assemble into a highly open 3D framework with ordered cylindrical channels (Fig. 12f). Öhrström *et al.*[21] reported a type of 1D Gd-MOF from the reaction of $Gd(NO_3)_3 \cdot 6H_2O$ with benzene-1,2,4,5-tetracarboxylate (H_4BTEC), 4,4′-azopyridine in a mixture of DMF and acetic acid. The central Gd^{3+} among the obtained CTH-16 [$Gd_2(BTEC)_2$] was coordinated by nine carboxylate oxygens from six different BTEC ligands (Fig. 12g), and the

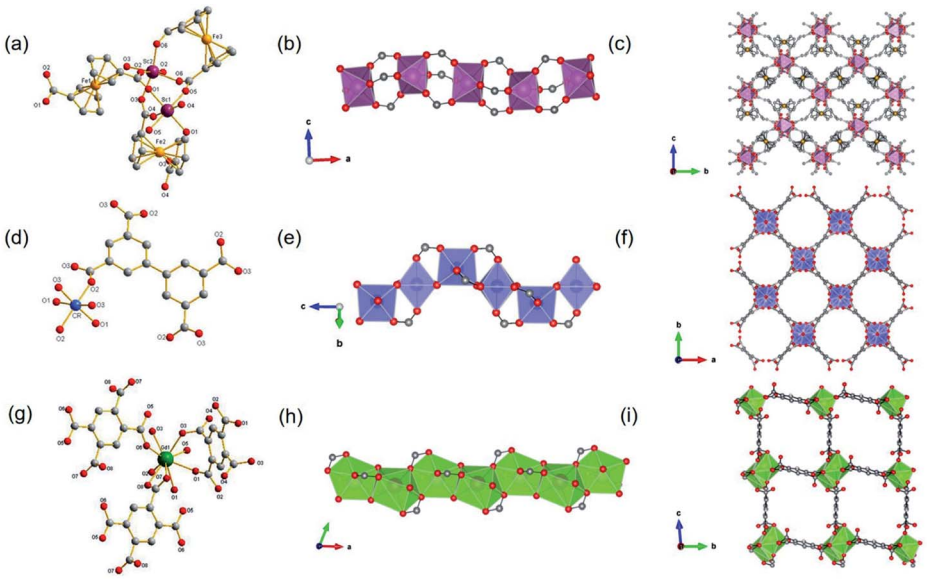

Fig. 12 (a) The coordination environment of Sc(III) ions among CAU-50; (b) The 1D infinite Sc–O chain extending along the *a*-axis; (c) the 3D framework structure of CAU-50 view down the *a*-axis. Reproduced with permission from ref. 99. Copyright 2020, Royal Society of Chemistry. (d) The coordination environment of Cr(III) ions among MFM-300(Cr); (e) the 1D chain structure formed by CrO_6 polyhedrons; (f) the 3D porous framework of MFM-300 projected down the *c*-axis. Reproduced with permission from ref. 31. Copyright 2014, Royal Society of Chemistry. (g) The coordination environment of Gd(III) ions among CTH-16; (h) the 1D chain ISBU pattern of CTH-16; (i) the [100] projection of 3D framework of CTH-16. Reproduced with permission from ref. 21. Copyright 2021, Elsevier Inc.

resulting GdO_9 polyhedron formed corresponding 1D Gd–O chain extending indefinitely along the *a*-direction through sharing polyhedron edges (Fig. 12h). Furthermore, adjacent chains were bridged by BTEC ligands to form a bi-nodal **htp** net with square-like open channels (Fig. 12i). Moreover, the same research group reported the 2D Ce(III)-MOF by reacting $Ce(NO_3)_3 \cdot 6H_2O$ with H_4BTEC in a mixture of DMF and acetic acid.[21] The obtained product (denoted as CTH-15 thereafter) had the molecular formula of $[Ce_3(BTEC)(HBTEC)(OAc)(HCO_2)]$ and crystallized in the monoclinic crystal system and the $P2_1/c$ space group. As shown in Fig. 13a, three symmetry-independent Ce(III) ions were observed with 10–12 oxygens-coordinated modes. With the Ce1–O polyhedra as the center, a polyhedral trimer was formed *via* the combination of one Ce2–O and Ce3–O polyhedron through sharing faces (Fig. 13b). As-formed polyhedral trimer was sequentially connected with each other *via* a face-to-face shared fashion along the *b*-axis and *via* an edge-by-edge shared fashion along the *c*-axis, thereby forming an infinite 2D Ce–O mesh structure within the *b*–*c* plane (Fig. 13c). Finally, adjacent Ce–O layers were connected by carboxylate groups of BTEC linkers to assembly into the 3D CTH-15 (Fig. 13d).

2.4 ISBU MOFs constituted of metal(IV) central ions

According to the classical hard-soft acids and bases (HSAB) theory, MOFs composed of tetravalent metals ions normally enjoy outcomes of the strong M(IV)–carbonate coordination,[12,101] like good thermal stability and chemical stability. To the best of our knowledge, ISBU MOFs based on metal(IV) elements are merely reported as examples of Ti(IV),[18,19,27,35–37,102] Zr(IV)[17,30,34,38,103–106] and Ce(IV),[105,107,108] which have been surveyed and introduced in this section.

In 2018, Serre *et al.*[27] carried out the reaction between $Ti(iPrO)_4$ (iPr = isopropoxide) and 5,5′-methylenediisophthalic acid (H_4MDIP) under reflux of formic acid to obtain 0D Ti-oxo-based $Ti_{12}O_{15}(MDIP)_3(formate)_6$ (MIL-177-LT), which further underwent phase transformation at 280 °C to produce MIL-177-HT with novel 1D Ti-oxo chains. MIL-177-HT featured the formula of $[(Ti_6O_9)_2(MDIP)_3]$ and crystallized in a hexagonal crystallographic system and the *P*6/mmm space group. Specifically, the 6-coordinated raw TiO_6 polyhedrons were connected to the Ti_6O_9 secondary clusters *via* sharing edges (Fig. 14a), which were further assembled into 1D infinite $[Ti_6O_9]_n$ chain *via* corner-sharing (Fig. 14b). Noteworthily, such titanium-oxo

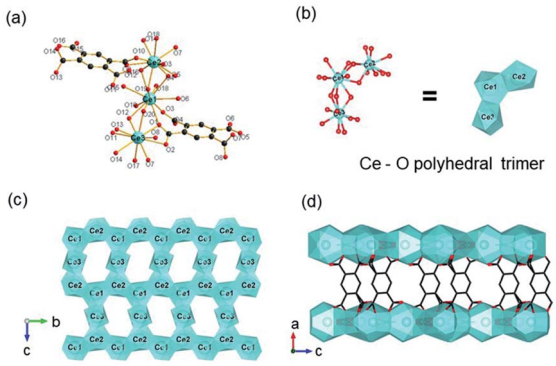

Fig. 13 (a) The coordination environment of Ce(III) ions among CTH-15; (b) the structure of Ce–O polyhedral trimer *via* face-sharing; (c) the 2D structure of CTH-15 growing within the *b*–*c* plane; (d) the channel distribution of CTH-15 projected along the *b*-axis. Reproduced with permission from ref. 21. Copyright 2021, Elsevier Inc.

hexamer was found identical to the unit structure of anatase TiO_2. After the connection of neighboring $[Ti_6O_9]_n$ chains by MDIP linkers, a 3D network with honeycomb channels (0.9 nm) was constructed finally (Fig. 14c).

After that, Chen *et al.*[18] synthesized a series of ZSTU MOFs characteristic of another type of 1D Ti-oxo chain. Taking ZSTU-1 $[Ti_6(\mu_3\text{-}O)_6(\mu_2\text{-}OH)_6(TCA)_2(H_2O)(DMF)_2]$ for the representation, it was synthesized by the solvothermal reaction of 4,4′,4″-nitrilotribenzoic acid (H_3TCA) and titanium isopropoxide in DMF at 180 °C for 24 h. The obtained ZSTU-1 crystallized in a hexagonal crystallographic system and $P6_3/mcm$ space group. In which, the Ti(IV) cation adopted an unusual 7-coordination fashion and was sequentially packed into a $Ti_6(\mu_3\text{-}O)_6(COO)_6$ subunit (Fig. 14d). Moreover, a 1D $[Ti(\mu_3\text{-}O)_6(\mu_3\text{-}OH)_6(COO)_6]_n$ chain was formed along the *c*-axis by six μ_3-OH-bridged connections of the hexamer subunits (Fig. 14e). In the *a*-*b* plane, the hexatopic $Ti_6(\mu_3\text{-}O)_6(COO)_6$ was further linked by the triangular TCA linker to form a (3,6)-connected **kgd** network with elliptical channels of 0.61 × 0.34 nm in dimensions (Fig. 14f). Isoreticular ZSTU-2 $[Ti_6(\mu_3\text{-}O)_6(\mu_2\text{-}OH)_6(BTB)_2(H_2O)(DMF)_2]$ and ZSTU-3 $[Ti_6(\mu_3\text{-}O)_6(\mu_2\text{-}OH)_6(BTCA)_2(H_2O)(DMF)_2]$ can be facilely obtained by using H_3BTB and H_3BTCA [tris(4′-carboxybiphenyl)amine] as organic ligands, respectively. Accordingly, the pore dimensions of ZSTU-2 and ZSTU-3 were enlarged to 0.85 × 0.46 nm and 1.37 × 0.71 nm, respectively.

In addition, the first 2D Ti-MOF example (denoted as COK-47s) was reported by Bueken *et al.*[19] COK-47s was synthesized by a microwave-assisted synthesis method involving heating H_2BPDC with Cp_2TiCl_2 (Cp = cyclopentadienyl) at 185 °C in the anhydrous mixed solvent of DMF and propylene carbonate. Among COK-47s, each Ti(IV) was coordinated to two carboxylate oxygen atoms, three μ_3-O oxygen atoms and one μ_2-O oxygen atom, and therefore adopted a TiO_6 octahedral mode, which was dimerized *via* sharing one edge (Fig. 14g). Furthermore, the dimer was condensed into infinite 2D Ti-oxo sheet structures by sharing edges along the *c*-axis and sharing corners along the *a*-axis, respectively (Fig. 14h). After the linkage of ditopic BPDC, adjacent sheets were assembled into the final 3D framework (Fig. 14i). The proposed 2D Ti-oxo sheet-based network was verified also applicable for terephthalic acid and 2,2′-bipyridine-5,5′-dicarboxylic acid, indications of the great potential for further modifications and functionalizations.

Thanks to the strong binding ability to carboxylate ligands, Zr(IV) MOFs usually exhibit robust thermal and chemical stabilities which are indispensable merits quested in versatile application fields.[12,104] The classical and famous OD $[Zr_6(\mu_3\text{-}O)_4(\mu_3\text{-}OH)_4]$ node contributes almost Zr(IV) MOFs and very few examples based on infinite Zr-oxo units have been reported to the best of our knowledgement.[105]

In 2016, Stock and his colleagues[38] used $ZrOCl_2 \cdot 8H_2O$ to react with 2,5-pyrazinedi-carboxylic acid (H_2PzDC) in a mixture of H_2O and formic acid at 120 °C for 24 h to produce the 1D CAU-22 with the formula of $[Zr_6(\mu_3\text{-}O)_4(\mu_3\text{-}OH)_4(\mu_2\text{-}OH)_2(PzDC)_3(OH)_2(H_2O)_2(HCO_2)_2]$. Among CAU-22, the 1D $[Zr_6O_4(OH)_4(\mu_2\text{-}OH)_2]_n$ rod was connected from discrete $[Zr_6O_4(OH)_4]$ octahedrons by μ_2-OH bridging along the *c*-axis (Fig. 15a and b). Moreover, each 1D chain was interconnected with six adjacent chains *via* six ditopic PzDC edges to build the final 3D framework (Fig. 15c). Later, the same research group reported another type of 1D Zr-MOF named as CAU-27,[17] which was obtained from phthalic acid and zirconium acetate under the acetic acid-based solvothermal conditions. Needle-like CAU-27 crystals with the formula of $[Zr_5O_4(OH)_4(OAc)_4(BDC)_2]$ belonged to the tetragonal system and $I4/mcm$ space group. In which, the 1D Zr-oxo chain grew from the infinite condensation of Zr-corner-shared $[Zr_6O_4(OH)_4]$ octahedrons along the *c*-axis (Fig. 15a and d). After linking by BDC at the sides, those chains were ultimately assembled into the corresponding tetragonal cell

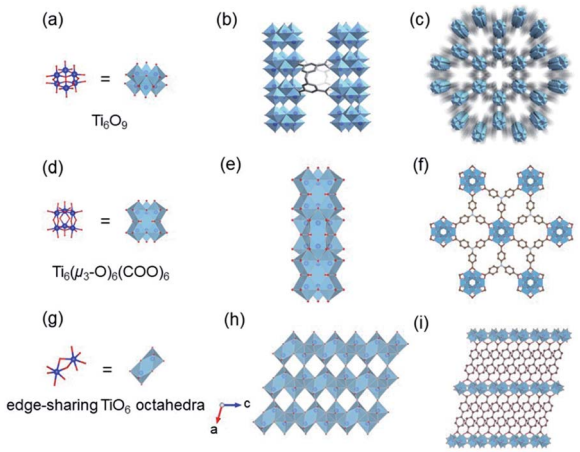

Fig. 14 (a) The structure of Ti_6O_9 cluster; (b) adjacent infinite $(Ti_6O_9)_n$ 1D chain connected by MDIP linker; (c) the 3D structure of MIL-177-HT. Reproduced with permission from ref. 27. Copyright 2018, Springer Nature Limited. (d) The structure of $Ti_6(\mu_3\text{-}O)_6(COO)_6$ unit; (e) the 1D infinite chain of ZSTU-1; (f) the open structure of ZSTU-1 projected at the [001] direction. Reproduced with permission from ref. 18. Copyright 2019, Royal Society of Chemistry. (g) The dimer of edge-sharing TiO_6 octahedrons; (h) the 2D sheet structure of COK-47 growing within the *a*–*c* plane; (i) the side view of COK-47. Reproduced with permission from ref. 19. Copyright 2019, WILEY-VCH Verlag GmbH.

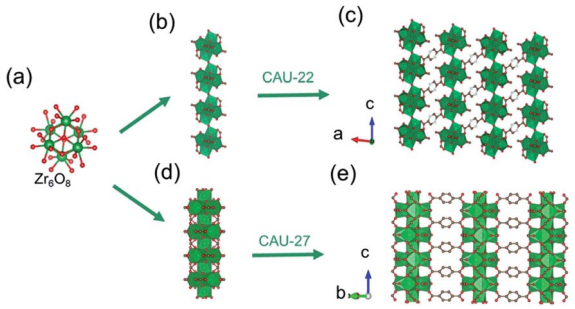

Fig. 15 (a) The structure of initial OD $[Zr_6(\mu_3\text{-}O)_4(\mu_3\text{-}OH)_4]$ cluster; (b) the infinite 1D Zr-oxo chain structure bridged by μ_2-OH; (c) corresponding framework structure of CAU-22. Reproduced with permission from ref. 38. Copyright 2016, Royal Society of Chemistry. (d) The infinite 1D Zr-oxo chain structure *via* sharing Zr corners; (e) corresponding framework structure of CAU-27. Reproduced with permission from ref. 17. Copyright 2019, WILEY-VCH Verlag GmbH.

(Fig. 15e) with part of the metal sites occupied by acetate terminals.

Distinct from the Zr_6O_8-condensed 1D chain introduced above, Devic *et al.*[106] reported a 1D Zr-MOF based on the novel Zr-oxo chain. The so-called MIL-163 [$Zr(H_2$-TzGal)] was synthesized from the reaction of 5,5′-(1,2,4,5-tetrazine-3,6-diyl)bis(benzene-1,2,3-triol) (H_6TzGal) and $ZrCl_4$ in DMF at 130 °C. Among MIL-163, the central Zr^{4+} adopted an 8-coordinated fashion with four carboxylate oxygens and four phenolic oxygens, and the as-formed ZrO_8 polyhedron (Fig. 16a) grew indefinitely along the *c*-axis to form corresponding Zr-oxo chains with shared edges (Fig. 16b). Together with the linkage of TzGal extending along both *a*- and *b*-axis (Fig. 16b), the open network with exposure of square channels was constructed as the final product. By replacing the ditopic H_6TzGal with tetratopic THPP (5,10,15,20-tetrakis(3,4,5-trihydroxyphenyl)porphyrin), Lin *et al.*[34] constructed novel ZrPP-1 [Zr_2(THPP)] featuring identical 1D Zr-oxo chains to MIL-163 in the water–DMF (v/v, 4/5) mixture at 140 °C. Distinctly, those 1D chains among ZrPP-1 were connected by the square-shaped THPP linkers and therefore formed a 4-connected **nbo** network (Fig. 16c).

In addition, Zhao *et al.*[30] reported the synthesis of Zr(IV)-MIL-140-4F reacted *via* heating $ZrCl_4$ and tetrafluoro-terephthalic acid (H_2TFBDC) in acetonitrile at 120 °C. Isoreticular to the well-known MIL-140 series,[105,108,109] the Zr(IV) cation adopted rare 7-connected coordination with four carboxylate groups and three μ_3-bridged oxygens atoms to form a ZrO_7 polyhedron (Fig. 16d). Sequentially, an infinitely Zr–O chain was obtained *via* edge-sharing those ZrO_7 polyhedrons in a zigzag way. The 3D network with 1D triangular channels (Fig. 16e) was constructed after the linkers installation in the *a*–*b* plane. More significantly, Ce(IV)-MIL-140-4F[107] with a similar $[CeO_7]_n$ zigzag chain was also obtained by simpling varying the metal precursor type. Recently, Huang *et al.*[32] further expanded such 1D chain-connected networks feasible for the tetra-connected tetrakis(4-carboxyphenyl)porphyrin (H_2TCPP) linker. The obtained PCN-226 [Zr_3O_3(TCPP)(benzoate)$_2$] crystallized in a higher symmetric orthorhombic crystallographic system and the *Ibam* space group due to the square geometry of TCPP. Among PCN-226, the edge-sharing zigzag ZrO_7 chain ran along the *b*-axis (Fig. 16d) and was further linked with metalloporphyrin linkers each other to form the final 3D framework of a new **ztt** topology (Fig. 16f).

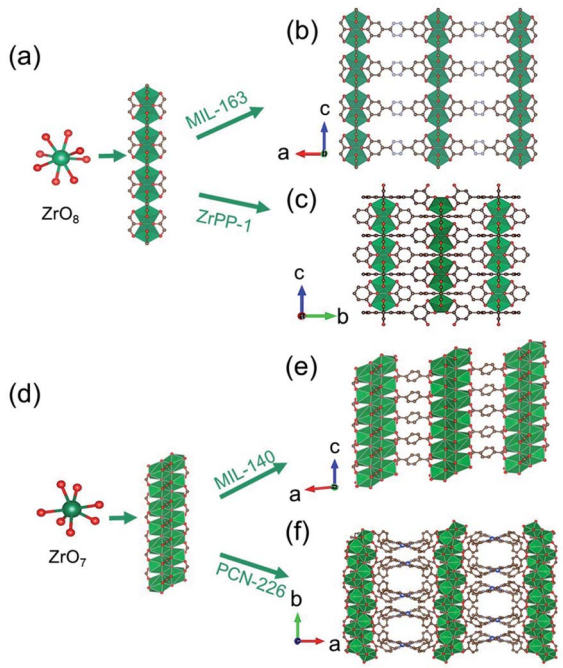

Fig. 16 (a) The infinite 1D Zr(IV)-oxo chain assembled from ZrO_8 polyhedrons; (b) corresponding framework structure of MIL-163. Reproduced with permission from ref. 106. Copyright 2015, WILEY-VCH Verlag GmbH. (c) The corresponding framework structure of ZrPP-1. Reproduced with permission from ref. 34. Copyright 2018, WILEY-VCH Verlag GmbH. (d) The infinite zigzag 1D Zr(IV)-oxo chain assembled from ZrO_7 polyhedrons; (e) corresponding framework structure of MIL-140. Reproduced with permission from ref. 30. Copyright 2021, WILEY-VCH Verlag GmbH. (f) The corresponding framework structure of PCN-226. Reproduced with permission from ref. 32. Copyright 2020, American Chemical Society.

3. Applications of ISBU MOFs

MOFs have drawn extensive application studies in fields of adsorption, gas separation, catalysis, energy storage and others, owing to their large surface area, tunable pore size, versatile functionalization ability, *etc.*[9,25,110–115] In this section, it is beyond our intention to summarize those application performances even based on ISBU MOFs, considering the innumerable examples reported so far. Rather, we have introduced and discussed their application performances by presenting some purposely selected ISBU MOFs, in order to highlight the unique physical and chemical properties enabled by corresponding ISBU structures.

3.1 Gas absorption

As a highly porous absorbent for gas uptake, the surface area and pore size of MOFs are well-known key factors determining their performances.[116–118] Besides, the recently developed series of 1D Al-MOFs featuring high gas uptake indicated the non-negligible function of unique 1D chain structures.[3,85,86] For example, MOF-303 featured with the 1D Al–O chain was reported as the world-record high uptake toward water adsorption (Fig. 17a).[3] The in-depth mechanism according to single-crystal X-ray diffraction (SXCRD) and theoretic simulation results deciphered that the unique 1D chain structure together with polar organic linkers played a major role. Enforced by densely packing of the 1D Al–O chain, adjacent pyrazole linkers, therefore, pointed toward each other closely accompanied by forming a hydrophilic pocket involved with three μ_2-OH dangling on the 1D chain and two N(H) on linkers. As the red region shown in Fig. 17a, a step adsorption isotherm was observed at very low pressure, corresponding to the formation of a four-water-assembled cluster inside such pocket by multiple and strong hydrogen bonding (Fig. 17b). Moreover, this water cluster acted as the seed for binding many more water molecules, which was

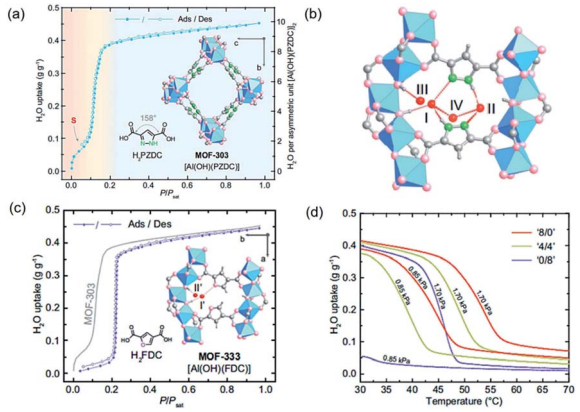

Fig. 17 (a) Water adsorption and desorption isotherms of MOF-303 at 25 °C. The three adsorption steps were shown in red, yellow, and blue in the background. Insets correspond to the structures of H_2PZDC and MOF-303; (b) the adsorption sites (I to IV) for the first to four water molecules inside the hydrophilic pocket; (c) water adsorption and desorption isotherms of MOF-333 at 25 °C. Insets showed H_2FDC structure and the first two adsorption sites inside the pocket of MOF-333; (d) the water vapor isotherms of homo- and mixed-ligand MOFs ('8/0', '4/4' and '0/8') at 0.85 to 1.70 kPa. Reprinted with permission from ref. 3. Copyright 2021, AAAS.

ascribed to the large water uptake of MOF-303 within a very small pressure range (yellow region shown in Fig. 17a). It is hence noteworthy to highlight that the dense layout of the hydrogen-bonding sites exposed on the infinite 1D Al–O chains together with adjacent pyrazole linkers cooperatively resulted in the hydrophilic pocket available for water cluster seeding and subsequent condensation. Full water adsorption of MOF-303 was accomplished at the saturation pressure with a maximum uptake of 0.45 g g^{-1}, which was a state-of-the-art performance in 2019. However, the strong hydrogen bonding on the other hand cast not easy desorption and regeneration of the harvested water, especially for waters captured before the S-step indicated in Fig. 17a. Hence, an isoreticular MOF-333 [Al(OH)(FDC)] with identical 1D Al–O chains but a less hydrophilic FDC linker instead, was constructed to control the hydrogen bonding toward water molecules. Compared with pyrazole, the less hydrophilic FDC made it weaker in hydrogen bonding with water molecules, as demonstrated by the absence of the corresponding S-step in the adsorption isotherm of MOF-333 but at a cost of much higher onset pressure (Fig. 17c). To achieve two birds with one stone, mixed PZDC and FDC ligands were adopted to construct the multivariate MOF for making a balance between the working capacity and regeneration ability. An optimized '4/4' (the molar ratio of PZDC to FDC) multivariate MOF exhibited excellent isobaric desorption performance at water vapor pressures of 0.85 to 1.70 kPa (corresponding to 20 to 40% RH at 30 °C), which was very practical for the water-harvesting system (Fig. 17d).

Normally, MOFs have been popularly quested for large CO_2 uptake.[108,119] Distinctly, Long *et al.*[28] reported appealing CO_2 triggered enantio-recognitions enabled by 1D Mg_2(DOBPTC) with helical Mg–O chain structures. With the assistance of chiral *trans*-1,2-diaminocyclohexane (dach), it was found that both the adsorption and desorption temperature of CO_2 selectively varied with the chiral conformation of the used Mg_2(DOBPTC) adsorbent. In combination with the experimental proofs and density functional theory (DFT) calculations, a unique chiral ammonium carbamate chain was formed *via* the co-condensation of the appended dach and the adsorbed CO_2, which further formed corresponding diastereomers with Mg_2(DOBPTC) of opposite chirality. Without double, the unique 1D Mg–O helical chain among Mg_2(DOBPTC) was recognized as the chiral template to trigger the chirality transfer. As shown in Fig. 18a, the space-filling models indicated a much tighter contact for (*R*,*R*)-dach-*R*-Mg_2(DOBPTC) in comparison to (*S*,*S*)-dach-*R*-Mg_2(DOBPTC). In accordance, the ammonium among (*R*,*R*)-dach-*R*-Mg_2(DOBPTC) also formed stronger hydrogen bonds with two different carboxylate oxygens with corresponding shorter N–H···O lengths than those among the (*S*,*S*)-dach-*R*-Mg_2(DOBPTC), as a further consolidation of the more favourable (*R*,*R*)-dach-*R*-Mg_2(DOBPTC) in thermodynamics (Fig. 18b). Experimentally, (*R*,*R*)-dach grafted racemic Mg_2(DOBPTC) presented two CO_2 desorption steps with distinct onset temperate, which could be assigned to the (*R*,*R*)-dach-*R*-Mg_2(DOBPTC) of higher desorption temperature and (*R*,*R*)-dach-*S*-Mg_2(DOBPTC) of relatively lower desorption temperature. By contrast, when the 50 : 50 (*R*,*R*) : (*S*,*S*) dach was used, racemic Mg_2(DOBPTC) presented only a single-step desorption curve with corresponding desorption temperature in between (Fig. 18c and d).

3.2 Gas separation

Thanks to the large specific surface area and adjustable pore size, MOFs have become one of the best promising materials for gas separation.[120–122] Isolation of CO_2 from acetylene (C_2H_2) is a long-standing challenge in the petrochemical industry arising from

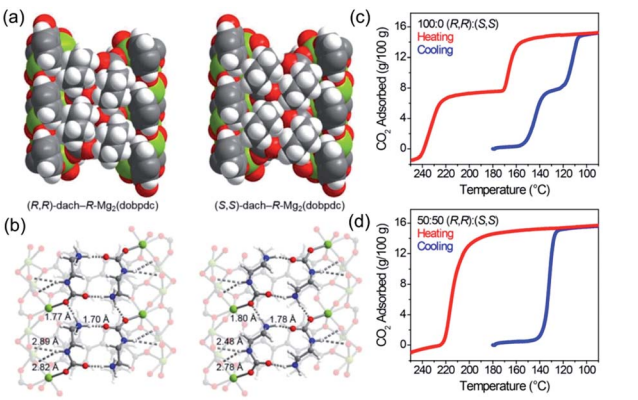

Fig. 18 (a) The space-filling models of (*R*,*R*)-dach-*R*-Mg_2(DOBPTC) and (*S*,*S*)-dach-*R*-Mg_2(DOBPTC); (b) the DFT-calculated structure parameters of the CO_2-insert (*R*,*R*)-dach-*R*-Mg_2(DOBPTC) and (*S*,*S*)-dach-*R*-Mg_2(DOBPTC). Element color: Mg is light-green, N is blue, O is red, C is gray, and H is white; (c and d) the thermogravimetric analyses of pure CO_2 isobars of Mg_2(DOBPTC) functionalized with different chiral dach isomers. Reprinted with permission from ref. 28. Copyright 2012, AAAS.

the nearly identical size, shape and physicochemical properties between the two gases. It was completely differentiated from the C_2H_2-preferred adsorption capabilities of conventional absorbents, inverse adsorption behavior was obtained by the 1D Ce(IV)-MIL-140-4F of trigonal-shaped ultramicroporous channels along with the exceptionally high CO_2/C_2H_2 selectivity.[30] There were electron-rich site I and electron-poor site II shown in the electrostatic potential distributions on the Hirshfeld surface of the Ce-MIL-140-4F (Fig. 19a) and the Zr-MIL-140-4F as a reference (Fig. 19b). In comparison to the Zr-MIL-140-4F counterpart, Ce(IV) with additional unoccupied 4f orbitals extracted electrons from the organic linker to the metal node more efficiently and thus offered a greater polarity on site I. Consequentially, a favorable uptake toward CO_2 (110.3 cm^3 cm^{-3} at 298 K, Fig. 19c) and inversed CO_2/C_2H_2 selectivity were conferred by Ce(IV)-MIL-140-4F *via* the strong host–guest interaction occurring at the site I. As another reference, Ce(IV)-UiO-66-4F phase comprising the same Ce(IV) and organic linker to Ce(IV)-MIL-140-4F, however, merely presented conventional C_2H_2/CO_2 separation selectivity (Fig. 19d), reflecting the potential contribution devoted by the unique 1D chain structure of Ce(IV)-MIL-140-4F. Likely, the condensed stacking fashion of polar organic linkers among 1D Ce(IV)-MIL-140-4F offered unique CO_2-favoured electrostatic potential distribution throughout the whole framework, which was absent in the case of 0D Ce(IV)-UiO-66-4F.

The CO_2 separation over N_2, another important industrial process used in the treatment of fuel gas, was tested by a rare pure Na-based 2D MOF-705 [Na_4(BDA)(CH_3OH)(H_2O), BDA = (2*S*,2′*S*)-2,2′-(terephthaloylbis (azanediyl))disuccinate].[45] MOF-705 featured infinite 2D sodium oxide sheets extending along its crystallographic *a*–*b* plane and showed uptakes of 65.0 and 3.1 cm^3 cm^{-3} toward adsorption of CO_2 and N_2, respectively, at 273 K and 800 Torr pressure. What's more, the breakthrough experiment was carried out in a mixture of 84% N_2 and 16% CO_2 to further show the practical potential of MOF-705. Promisingly, MOF-705 could adsorb CO_2 specifically with the capture efficiency over 98% and at the same time interact with N_2 negligibly. The adsorbed CO_2 in pores of MOF-705 could be removed simply by flowing pure N_2 at room temperature and the regenerated material could be repeatedly used for at least three cycles without obvious performance decline.

Metal-mixing is a common but effective strategy to enhance performances by combining both merits of the homometallic analogies.[20,31,123] Schroder and his colleagues[31] constructed a heterometallic 1D MFM-300($Al_{0.67}Cr_{0.33}$) for SO_2 separation from CO_2, which was compared in parallel to its homometallic MFM-300(Al) and MFM-300(Cr). According to the experimental results, MFM-300(Al) showed both stronger adsorption toward SO_2 and CO_2 but at the compromise of lower SO_2/CO_2 selectivity than MFM-300(Cr). In between, heterometallic MFM-300($Al_{0.67}Cr_{0.33}$) inherited high SO_2 uptake up to 8.59 mmol g^{-1} at 273 K and 1 bar pressure (Fig. 20a), and meanwhile an appreciable SO_2/CO_2 selectivity (Fig. 20b). The overall superior performance achieved by MFM-300($Al_{0.67}Cr_{0.33}$) has been attributed to the interaction strength between its 1D chain (Al-μ_2OH–Cr) with adsorbents. A shorter binding length was found for μ_2OH···OSO (3.163 Å) in the case of MFM-300($Al_{0.67}Cr_{0.33}$) compared with the homometallic ones, meaning the stronger SO_2 interaction of MFM-300($Al_{0.67}Cr_{0.33}$) (Fig. 20c and d). In

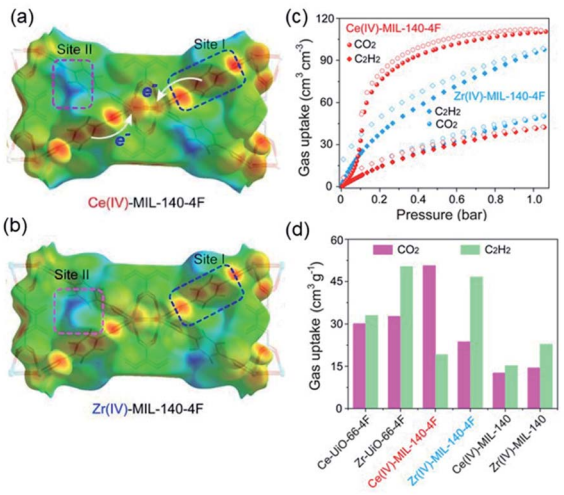

Fig. 19 The electrostatic potential distributions on the Hirshfeld surface of (a) Ce-MIL-140-4F and (b) Zr-MIL-140-4F (red-to-blue color indicates the high-to-low transition of electron density); (c) the CO_2 and C_2H_2 isotherms of Ce(IV)- and Zr(IV)-MIL-140-4F collected at 298 K; (d) the CO_2 and C_2H_2 uptakes of different MOF samples at 298 K. Reprinted with permission from ref. 30. Copyright 2021, WILEY-VCH Verlag GmbH.

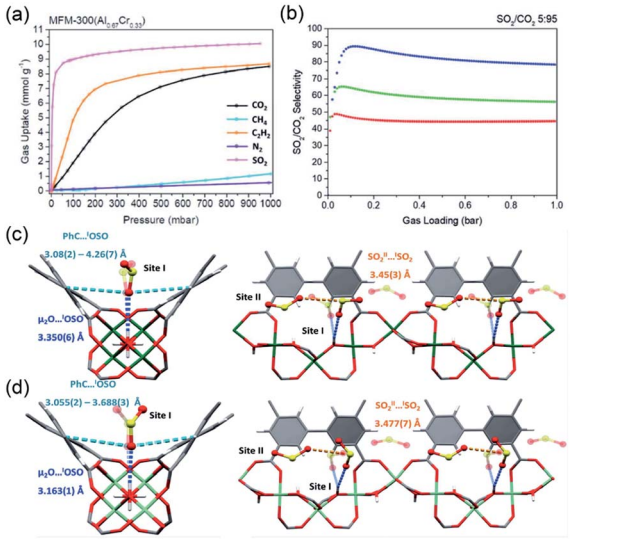

Fig. 20 (a) The adsorption isotherms toward CO_2 (black), CH_4 (aqua), C_2H_2 (orange), N_2 (purple) and SO_2 (pink) of MFM-300($Al_{0.67}$Cr0.33), at 273 K; (b) the ideal adsorbed solution theory (IAST) selectivity of SO_2/CO_2 (5 : 95) achieved by MFM-300(Al) (red), MFM-300($Al_{0.67}Cr_{0.33}$) (green) and MFM-300(Cr) (blue) up to 1 bar at 273 K. Views of binding of SO_2^{I} and of $SO_2^{I}\cdots SO_2^{II}$ interactions among (c) MFM-300(Cr) and (d) MFM-300($Al_{0.67}Cr_{0.33}$). Element color: Cr is green, AlCr is light green, S is yellow, O is red, C is grey, H is white. Bond color: μ_3-OH···OSO^{I} is blue bond, Ph···SO_2^{I} is turquoise bond, $SO_2^{I}\cdots SO_2^{II}$ interactions is orange bond. Reprinted with permission from ref. 31. Copyright 2021, Royal Society of Chemistry.

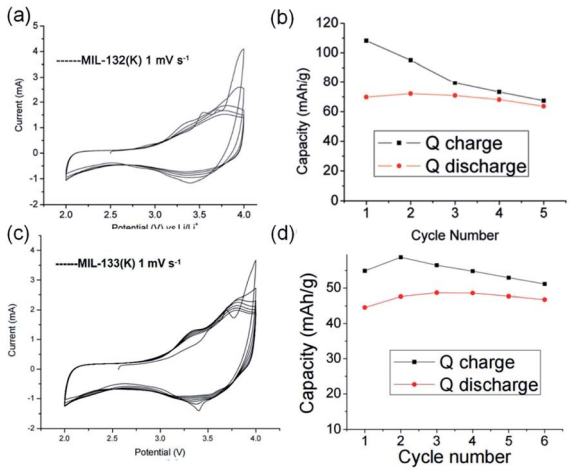

Fig. 21 (a) The solid-state cyclic voltammetry of MIL-132K between the 2 and 4 V *vs.* Li/Li^+ at 1 mV s^{-1}; (b) the charge and discharge capacity of MIL-132K within 5 cycles; (c) the solid-state cyclic voltammetry of MIL-133K between the 2 and 4 V *vs.* Li/Li^+ at 1 mV s^{-1}; (d) the charge and discharge capacity of MIL-132K within 6 cycles. Reprinted with permission from ref. 44. Copyright 2010, American Chemical Society.

addition, the intermediate SO_2/CO_2 selectivity was clued by the guest–guest packing alongside the 1D chain, as one can see a minorly loose $SO_2\cdots SO_2$ distance (3.477) found in the MFM-300($Al_{0.67}Cr_{0.33}$) than that (3.45) of MFM-300(Cr) of the best selectivity.

3.3 Energy-related application

By taking the advantages of rich active sites, low resistance of mass transport and easy alternation of functionality, MOFs are also promising candidates for energy storage,[124] like being used as, the active electrodes for batteries[32,44,125–128] and the proton-conductive membrane[27,58,129–131] used in fuel cells.[132,133] More than those, the unique ISBU structures can bring additional merits (*e.g.*, higher energy density and improved performance stability), as compared with conventional OD MOFs. As a proof of concept, the ID MIL-132(K) and 2D MIL-133(K) both composed of redox-active TTF linkers (corresponding crystal structures have been specifically described in Fig. 21a) were used as cathode materials in Li-ion batteries.[44] Based on the solid-state cyclic voltammetry at a scanning rate of 1 mV s^{-1}, the 1D MIL-132K exhibited a reversible redox couple between 2.0 and 4.0 V *vs.* Li/Li^+, giving rise to an initial charge capacity of nearly 110 mA h g^{-1} (Fig. 21b). Similar redox coupling was also observed for MIL-133K but corresponding to a much lower capacity of 55 mA h g^{-1}, owing to the densely packed 2D K–O sheet unfavorable for Li-ions insertion and diffusion. But, a better cycling performance was achieved by the 2D MIL-133K on basis of its more robusticity, as seen from the nearly unchanged capacity after 6 concussive cycles (Fig. 21c). In sharp contrast, the charge capacity of the 1D MIL-132(K) declined to about half of the initial one after only 5 cycles (Fig. 21d).

MOFs of good proton conductivities have been nominated as promising membranes used in fuel cells. Mak *et al.*[129] synthesized a 1D [Sr_2(BPTC)$(H_2O)_6$, denoted as Sr-MOF-3] featuring hydrophilic channels (Fig. 22a). Water molecules were captured inside Sr-MOF-3 and self-assembled into heptamer-based networks *via* the interaction with ligated oxygen atoms on the 1D Sr–O chain and carboxylate oxygens from BPTC. Undoubtedly, the specific 1D Sr–O chain acted as the template for the construction of a straightforward hydrophilic path for acquiring good proton conductivity (Fig. 22b). Nyquist plots of Sr-MOF-3 showed an optimum proton conductivity of 2.7×10^{-4} S cm^{-1} at 98% and 90 °C (Fig. 22c). More recently, Yang *et al.*[58]

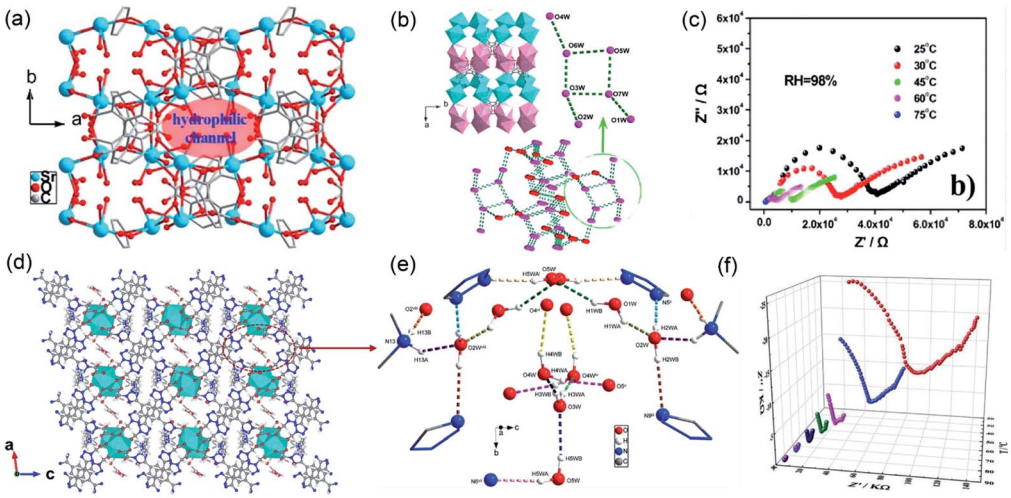

Fig. 22 (a) The crystal structure of 1D [Sr_2(BPTC)$(H_2O)_6$], H atoms are omitted for clarity; (b) polyhedral structure diagram of 1D Sr–O chain. Hydrogen bonding networks composed of water molecules (pink) and carboxylate oxygen atoms (red); (c) the impedance spectra of 1D [Sr_2(BPTC)$(H_2O)_6$] from 25 to 75 °C at 98% RH. Reprinted with permission from ref. 129. Copyright 2014, American Chemical Society. (d) The 3D framework structure of Ba-MOF-1, the part marked is the hydrogen-bonding networks formed in the channel; (e) hydrogen-bonding networks formed in the 1D channels of Ba-MOF-1; (f) the impedance spectra of Ba-MOF-1 from 25 to 85 °C at 98% RH. Reprinted with permission from ref. 58. Copyright 2021, Royal Society of Chemistry.

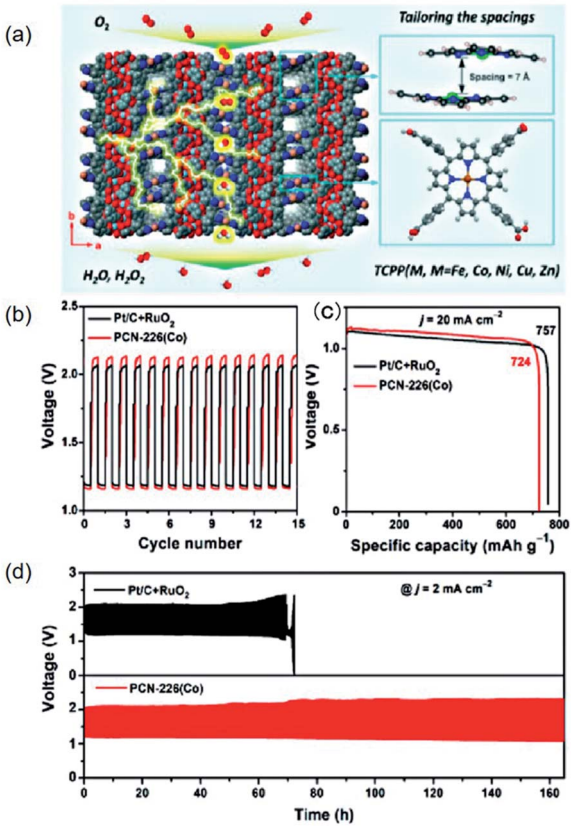

Fig. 23 (a) The schematic of the mechanism of PCN-226(Co) as a redox electrocatalyst in ORR; (b) cycle curves of PCN-226 and commercial Pt/C + RuO_2 for discharge and charge in the zinc–air cell. (c) The discharge curves of PCN-226(Co) and commercial Pt/C + RuO_2 at the current density of 20 mA cm^{-2}. (d) Long-term durability test of the Zn–air batteries at the current density of 2 mA cm^{-2} assembled with PCN-226(Co) and commercial Pt/C + RuO_2 active electrode, respectively. Reprinted with permission from ref. 32. Copyright 2020, American Chemical Society.

constructed a 1D Ba-MOF-1 (detailed crystal structure is available in Fig. 5) for proton-conducting. The densely packed Ba–O 1D chain together with the also closely spaced polar tetrazole rings triggered the formation of strong intermolecular hydrogen-bonding networks involved with O_w–H···O, O_w–H···N, N–H···O, C–H···N and C–H···O inside the hydrophilic 1D channel (Fig. 22d and e). The alternating current (AC) impedance spectrum (Fig. 22f) showed that a pronounced proton conductivity equal to 1.72×10^{-4} S cm^{-1} was acquired by robust moisture and thermal stabilities, and a further improved conductivity of 4.47×10^{-3} S cm^{-1} was achieved by Ba-MOF-1 Ba-MOF-1 at 98%RH and 25 °C. By fully taking advantage of once testing the sample at 85 °C.

Metalloporphyrinic MOFs have been widely tested in hydrogen evolution reaction (HER),[125,134] carbon dioxide reduction reaction (CO_2RR),[34] oxygen-involved reduction (ORR)[32] and evolution reaction (OER).[135] Nevertheless, challenges still stand in terms of acquiring high current density and long-term performance stability. As high surface area as well as large porosity offered by conventional OD MOFs are always compromised of the risk of framework collapses. Huang *et al.*[32] recently reported a novel PCN-226 comprising 1D infinite $[ZrO_7]_n$ chain and densely packed metalloporphyrinic linkers (TCPP M, M = Fe, Co, Ni, Cu, Zn, detailed structure description is available in Fig. 23a), which exhibited excellent electrocatalytic activity and good longevity in ORR by virtue of its unique 1D $[ZrO_7]_n$ chain. After coating the PCN-226 catalyst on carbon cloth, the assembled cell exhibited an open-circuit voltage of 1.37 V, and discharge/charge voltages of 1.17/2.14 V, respectively (Fig. 23b). The corresponding specific capacity of PCN-226(Co) was calculated as 724 mA h g^{-1}, comparable to 757 mA h g^{-1} for the commercially available Pt/C + RuO_2 catalyst (Fig. 23c). More significantly, thanks to the robust 1D chain structure, the PCN-226-based cell maintained a no obvious performance degradation over 160 h, surpassing the 60 h of Pt/C + RuO_2 by far (Fig. 23d).

3.4 Photocatalysis

The versatile chemistries of both metal nodes and organic linkers enable MOFs as promising photocatalysts with tunable band structures.[136–139] Nevertheless, further advancing MOFs in practice is hampered by their ultralow charge separation efficiencies and much inferior charge mobilities to commercial inorganic semiconductors. Distinct from majorities of OD samples, photoactive MOFs based on ISBUs are suggested to behave more like corresponding metal-oxide semiconductors.[18,19,27,35] For instance, Serre *et al.*[27] reported the exceptional photoconductivity of novel 1D titanium-oxo MOF (MIL-177-HT), which has exhibited comparably high charge mobility to semiconductive TiO_2 in addition to its excellent stability and high porosity. MIL-177-HT was obtained from the thermal-induced phase transformation of 0D $Ti_{12}O_{15}$ cluster-based MIL-177-LT (Fig. 24a). Note that, the resulting 1D $(Ti_6O_9)_n$ chain among MIL-177-HT presented an unprecedented high condensation degree of 1.5 among all reported Ti-MOFs,

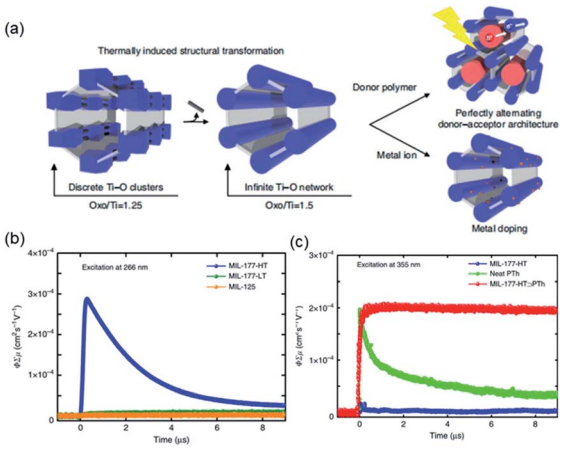

Fig. 24 (a) The schematic of the phase transformation and modification of MIL-177 structure; (b) transient conductivity of FP-TRMC under 266 nm laser excitation; (c) transient conductivity of FP-TRMC under 355 nm laser irradiation. Reproduced with permission from ref. 27. Copyright 2018, Springer Nature Limited.

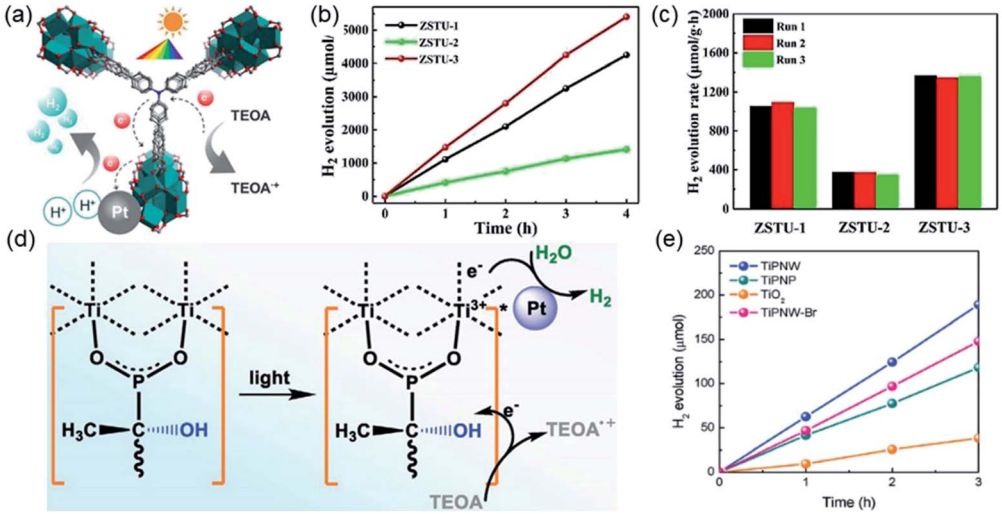

Fig. 25 (a) Schematic diagram of photocatalytic hydrogen evolution mechanism of ZSTU MOFs; (b) the amount of H_2 produced by ZSTU-1, ZSTU-2 and ZSTU-3 under visible light irradiation ($\lambda > 420$ nm); (c) recovery performance of ZSTU-1, ZSTU-2 and ZSTU-3 in the photocatalytic hydrogen evolution reaction under visible light irradiation for three times. Reprinted with permission from ref. 18. Copyright 2019, Royal Society of Chemistry. (d) Mechanism diagram of TiPNW photocatalytic hydrogen evolution reaction. (e) The photocatalytic hydrogen evolution activity under visible light irradiation. Reprinted with permission from ref. 34. Copyright 2020, WILEY-VCH Verlag GmbH.

an indictor of structure closing to pure inorganic TiO_2 with a condensation degree of 2.0. In the flash photoluminescence time-resolved microwave conductivity (FP-TRMC) testing, MIL-177-HT exerted very significant signs up to 3×10^{-4} cm^2 s^{-1} V^{-1} under ultraviolet light (266 nm) excitation, a comparable value as high as traditional TiO_2 semiconductors.

In sharp contrast, OD MIL-177-LT and familiar MIL-125 with the condensation degree of 1.25 and 1.0, respectively, both gave negligible photoresponse due to the absence of related 1D conduction chains (Fig. 24b). Further performance improvement could be facilely achieved *via* doping electron-donative polymers or metal ions. Taking the former for representation, MIL-177-HT⊃PTh (PTh = polythiophene) composite exhibited remarkably improved photoconductivity under excitation of 355 nm than neat MIL-177-HT. More significantly, a much-prolonged decay lifetime was observed for MIL-177-HT⊃PTh compared with pure PTh, indicating the facilitated charge separation process (Fig. 24c). Recently, another Ti-MOF [TiO_2(-TBAPy), TBAPy = 4,4′,4″,4‴-(pyrene-1,3,6,8-tetrayl) tetrabenzonate], denoted as ACM-1,[37] was reported with its energy band dispersion alongside the corner-shared 1D $[TiO_6]_n$ octahedral chain. Hence, the high mobility of photoinduced electrons together with a long charge separation lifetime guaranteed the excellent performance of ACM-1 in both photocatalytic hydrogen evolution and selective oxidation of organics.

What's more, the easy tunability of organic linkers is also facile for performance regulation.[18,35] Chen *et al.*[18] used H_3TCA, H_3BTB and H_3BTCA to construct 1D Ti-oxo ZSTU-1, ZSTU-2 and ZSTU-3 (corresponding crystal structures are described in Fig. 10), respectively, in the application of photo-induced hydrogen evolution (Fig. 25a). Using Pt nanoparticles (NPs) as the co-catalyst and triethanolamine (TEOA) as the sacrificial agent, ZSTU-1 and ZSTU-3 exhibited much higher performance than ZSTU-2 (Fig. 25b) thanks to the photoactive triphenylamine segment giving response to the visible light. In comparison to ZSTU-1, ZSTU-3 still showed slightly improved activity due to the extended conjugation system in H_3BTCA. It deserves to highlight that the hydrogen evolution rate (1350 μmol g^{-1} h^{-1}) achieved by 1D ZSTU-3 was more than double that of the OD MIL-125-NH_2, mightily due to the much faster charge mobility of 1D ISBU. In addition, three MOF catalysts all exerted excellent performances after three concussive testing cycles thanks to their robust 1D inorganic chains (Fig. 25c).

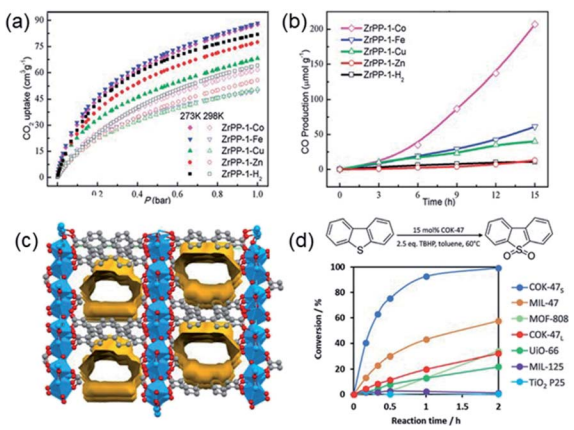

Fig. 26 (a) CO_2 adsorption of ZrPP-1-M (M = Co, Fe, Cu, Zn, H_2) at different temperatures; (b) reduction process of CO_2 to CO with ZrPP-1-M catalyst under visible light irradiation. Reprinted with permission from ref. 34. Copyright 2018, WILEY-VCH Verlag GmbH. (c) The visualized pore structure of COK-47, resulting in approximately 6 Å pores due to lack of connectives; (d) conversion rates of different catalysts in the photooxidation of DBT. Reprinted with permission from ref. 19. Copyright 2019, WILEY-VCH Verlag GmbH.

Table 1 Summarized information of the recently reported ISBU MOFs

No.	MOF	Metal	ISBU	ISBU composition	Formula	Coordination polyhedron	Crystallography system	Space group	Topology	Properties & applications	Ref.
1	IMP-24Li	Li(I)	1D	$[LiO_6]_n$	Li_4L1(4,4′,4"-(methylsilanetriyl)tribenzoate)DMF	LiO_6	Trigonal	$P3_121$		CO_2 uptake: 32.4 wt% at 500 °C	42
2	ULMOF-1	Li(I)	2D	$[LiO_4]_n$	Li_2(naphthalene-2,6-dicarboxylate)	LiO_4	Monoclinic	$P2_1/c$		Decomposition $T = 610$ °C	26
3	ULMOF-2	Li(I)	2D	$[LiO_4]_n$	Li_2(4,4-bisphthalboxylate)	LiO_4	Monoclinic	$P2_1/c$		Decomposition $T = 575$ °C	43
4	IMP-27Na	Na(I)	1D	$[NaO_6]_n$	Na_4(4,4′,4″,4‴-silanetetrayltetrabenzoate)$(H_2O)_4$	NaO_6	Triclinic	$P\bar{1}$			42
5	MOF-705	Na(I)	2D	$[NaO]_n$	Na_4[(2*S*,2′*S*)-2,2′-(terephthaloylbis(azanediyl)) disuccinate]$(CH_3OH)(H_2O)$	$Na1O_5$, $Na2O_4$, $Na3O_4$, $Na4O_6$	Monoclinic	$P2_1$		CO_2/N_2 separation, Sel. = 20.9	45
6	MOF-706	Na(I)	2D	$[NaO]_n$	Na_4[(2*S*,2′*S*)-2,2′-(1,1′-biphenyl)-4,4′(dicarbonyl) bis(azanediyl)disuccinate])$(CH_3OH)(H_2O)$	$Na1O_5$, $Na2O_4$, $Na3O_4$, $Na4O_6$	Monoclinic	$P2_1$		CO_2/N_2 separation, Sel. = 20.5	45
7	MIL-132	K(I)	1D	$[KO_5]_n$	K_2H_2(redox tetracarboxylic acid)	KO_5	Monoclinic	$P2_1/c$		Li-ion battery, initial charge capacity = 110 mA h g^{-1}	44
8	MIL-133	K(I)	2D	$[KO_4]_n$	M_2H_2(redox tetracarboxylic acid) (M = K^+ or Rb^+)	KO_4	Orthorhombic	*Pnmm*		Li-ion battery, initial charge capacity = 55 mA h g^{-1}	44
9	Cu(I)-MOF	Cu(I)	1D	$[CuI]_n$	Cu_6I_6(1,4-bis(phenylthio)but-2-yne)$_3$	CuI	Orthorhombic	*Pbca*		Thermoelectric composites	48
10	PbCu-MOF-1	Pb(II)	1D	$[PbO]_n$	$Pb_4Cu_2I_2$(3,5-pyridinedicarboxylate)$_4$$(DMF)_6$	$Pb1O_8$, $Pb2O_5$	Monoclinic	$P2_1/c$		Luminescence ratiometric thermometer	75
11	KGF-1	Pb(II)	3D	$[PbS_5N_2]_n$	Pb_3(Trithiocyanuric acid)$_2$·$2H_2O$	$Pb1S_4N_2$, $Pb2S_5N_2$	Monoclinic	$P2_1/c$		Decomposition $T = 390$ °C, conductivity = 7.4×10^{-5} cm^2 V^{-1} s^{-1}	22
12	AgPb-MOF	Pb(II)	2D	$[AgPbO]_n$	Ag_2Pb_2(1,3,5-benzenetricarboxylic acid)$_2$	AgO_5, PbO_7	Triclinic	$P\bar{1}$		Decomposition $T = 320$ °C	80
13	Pb-MOF	Pb(II)	2D	Pb–O–Pb	Pb_5(1,4-benzenedicarboxylate)$_4$$(OAc)_2$	$Pb1O_6$, $Pb2O_8$, $Pb3O_8$	Triclinic	$P\bar{1}$		CO_2 uptake: 25.8 cm^3 cm^{-1} at 298 K	140
14	Mg-MOF-74	Mg(II)	1D	$[MgO_6]_n$	Mg_2(3,3′-dihydroxy-[1,1′-biphenyl]-4,4′-dicarboxylic acid)	MgO_6	Trigonal	$R\bar{3}$		Adjustable ultra-large aperture: 14–98 Å	10
15	Mg-MOF	Mg(II)	1D	$[MgO_6]_n$	Mg_2(4,4′-di-oxidobiphenyl-3,3′-dicarboxylate)	MgO_6	Trigonal	$P3_221$		CO_2 enantioselective adsorption	28
16	CPF-1	Mg(II)	1D	$[MgO_6]_n$	$Mg_2(H_2O)_2$(3,3′,5,5′-tetracarboxylate)	MgO_6	Tetragonal	$I4_122$			51
17	Mg-MOF-1	Mg(II)	3D	$[MgO_6]_n$	Mg_3(formic acid)$_6$	MgO_6	Monoclinic	$P2_1/c$		Decomposition $T = 417$ °C	71
18	Mg-BPTC	Mg(II)	1D	$[MgO_6]_n$	[Mg(2,2,6,6-tetracarboxybipheny)$_{0.5}$$(H_2O)_3$]·$5H_2O$	MgO_6	Monoclinic	$C2/c$		Proton conductivity = 2.6×10^{-4} S cm^{-1} at 100 °C and 98% RH	129
19	Ca-MOF-1	Ca(II)	1D	$[CaO]_n$	Ca_3(1,3,5-tris(4-carboxyphenyl)benzene)$_2$	$Ca1O_6$, $Ca2O_7$	Trigonal	$R3$		Blue fluorescence	53
20	Ca-MOF-2	Ca(II)	1D	$[CaO_8]_n$	Ca(1,4-benzenedicarboxylate)(DMF)(OH_2)	CaO_8	Monoclinic	$P2_1/c$		Blue fluorescence	53
21	Ca-MOF-3	Ca(II)	2D	$[CaO_7]_n$	$Ca_2(OH)_2$(2,6-naphathalenedicarboxylate)	CaO_7	Monoclinic	$P2_1/c$			66
22	Ca-MOF-4	Ca(II)	2D	$[Ca_3O_{19}]$n	Ca_3(5-bromoisophthalic acid)$_3$$(H_2O)_3$·$H_2O$	$Ca1O_7$, $Ca2O_7$, $Ca3O_9$	Monoclinic	$P2_1/c$		Decomposition $T = 240$ °C	62

Table 1 (*Contd.*)

No.	MOF	Metal	ISBU	ISBU composition	Formula	Coordination polyhedron	Crystallography system	Space group	Topology	Properties & applications	Ref.
23	Ca-MOF-5	Ca(II)	1D	$[CaOCa]_n$	$[H_2N(CH_3)_2]Ca_7$(1,3,5-tris(4-carboxyphenyl) benzene)$_5$-$(H_2O)_8(DMF)_4]\cdot 4H_2O$	$Ca1O_7$, $Ca2O_9$	Monoclinic	$C2/c$			54
24	Sr-MOF-1	Sr(II)	1D	$[SrO_8]_n$	Sr(1,4-benzenedicarboxylate)(H_2O)(DMF)	SrO_8	Monoclinic	$P2_1/c$		Decomposition $T = 328$ °C, C_2H_2 uptake: 185.50 $cm^3\ g^{-1}$ at 298 K	57
25	Sr-MOF-2	Sr(II)	2D	$[SrO]_n$	$Me_2NH_2]_2[Sr_5$(1,3,5-benzenetricarboxylate$)_4(H_2O)_5$	$Sr1O_8$, $Sr2O_8$, $Sr3O_{10}$	Orthorhombic	$C222_1$		Decomposition $T = 100$ °C	67
26	Sr-MOF-3	Sr(II)	1D	$[SrO]_n$	$[Sr_2$(2,2,6,6-tetracarboxybipheny$)(H_2O)_6]\cdot H_2O$	$Sr1O_8$, $Sr2O_9$	Monoclinic	$P2_1/c$		Proton conductivity $= 2.7 \times 10^{-4}$ S cm^{-1} at 98% RH and 90 °C	129
27	Sr-MOF-4	Sr(II)	1D	$[Sr_5O_{28}]$n	$[H_2N(CH_3)_2]_2Sr_5(H_2O)_6$(1,3,5-tris(4-carboxyphenyl) benzene$)_4$	SrO_8	Monoclinic	$C2/c$			54
28	CAUMOF-8	Sr(II)	3D	$[SrO]_n$	Sr_2(1,3,5-benzenetricarboxylic$)(NO_3)$	$Sr1O_9$, $Sr2O_8$	Hexagonal	$P\text{-}6_2/c$		Decomposition $T = 500$ °C	72
29	Ba-MOF-1	Ba(II)	1D	$[BaO_{10}]_n$	$Me_2NH_2]$[Ba(1,3,5-tri(2-carboxymethyltetrazol-5-yl) benzene$)(H_2O)$	BaO_{10}	Monoclinic	$C2/c$		Proton conductivity: 1.72 $\times 10^{-4}$ S cm^{-1} at 98% RH and 85 °C	58
30	Ba-MOF-2	Ba(II)	1D	$[BaO_8]_n$	Ba(NH_2–1,4-benzenedicarboxylate)(DMF)	BaO_8	Trigonal	$P3_1$		Decomposition $T = 300$ °C	53
31	Ba-MOF-3	Ba(II)	2D	$[BaO]_n$	$[Me_2NH_2^+]_2$ [Ba_5(3,3′,5,5′-biphentetrolate$)_3(H_2O)_6$]	$Ba1O_{10}$, $Ba2O_9$	Tetragonal	$P6/m$		Decomposition $T = 540$ °C	68
32	Ba-MOF-4	Ba(II)	3D	$[BaO]_n$	Ba_3(1,3,5-benzenetricarboxylic$)_2(H_2O)_4$	$Ba1O_7$, $Ba2O_8$, $Ba3O_9$	Orthorhombic	$Pna2_1$		Decomposition $T = 500$ °C	70
33	Ba-MOF-6	Ba(II)	2D	$[BaO]_n$	Ba_2(3,6-dibromobenzene-1,2,4,5-tetracarboxylic acid$)(H_2O)_2$	BaO_{10}	Orthorhombic	$Cmce$		Decomposition $T = 370$ °C	65
34	Ba-MOF-7	Ba(II)	2D	$[Ba_3(\mu_4\text{-}NO_3)_2(\mu_3\text{-}Cl)]_n$	$Ba_3(\mu_5$-2-(hydroxymethyl)-1H-imidazole-4,5-dicarboxylicacid$)(\mu_5$-2-(hydroxymethyl)-1H-imidazole-4,5-dicarboxylicacid$)(\mu_4\text{-}NO_3)_2(\mu_3$-Cl)	$Ba1ClO_8$, $Ba2ClNO_8$	Orthorhombic	$Fdd2$		Decomposition $T = 330$ °C	64
35	Ba-MOF-8	Ba(II)	1D	$[BaO_9]_n$	$[H_2N(CH_3)_2]Ba(H_2O)$(1,3,5-tris(4-carboxyphenyl) benzene)	BaO_9	Orthorhombic	$Pna2_1$		SHG response, ferroelectric and piezoelectric properties	54
36	Ba-BPTC	Ba(II)	1D	$[BaO]_n$	$[Ba_6$(2,2,6,6-tetracarboxybipheny$)_3(H_2O)_6]\cdot 11H_2O$	$Ba1O_7$, $Ba2O_8$, $Ba3O_9$	Monoclinic	$P2_1/c$		Water stability over one month	129
37	Ba-MOF-9	Ba(II)	1D	$[BaO_9]_n$	$[Ba_2$(*N*,*N*-di(2-carboxymethyltetrazol-5-yl) amine$)_2(H_2O)_5]\cdot 2H_2O$	BaO_9	Triclinic	$P\bar{1}$		Decomposition $T = 260$ °C	58
38	Ba-MOF-10	Ba(II)	1D	$[Ba(CO_2)_3Ba]_n$	(Me_2NH_2)[Ba(1,3,5-tri(2-carboxymethyltetrazol-5-yl) benzene$)(H_2O)]\cdot 3H_2O$	BaO_{10}	Monoclinic	$P2_1/c$		Proton conductivity $= 4.47 \times 10^{-3}$ S cm^{-1} at 85 °C and 98% RH	58
39	Ba-MOF-11	Ba(II)	1D	$[BaO_9]_n$	$[Ba_3(\mu_2\text{-}H_2O)$(4,5-di(tetrazol-5-yl)imidazolylacetic acid$)_2(H_2O)_3]\cdot 2H_2O$	BaO_9	Triclinic	$P\bar{1}$		Decomposition $T = 204$ °C	58
40	Ba-MOF-12	Ba(II)	1D	$[BaO_9]_n$	Ba(3,5-pyrazoledicarboxylic acid$)H_2O$	BaO_9	Monoclinic	$P2_1/c$		Catalytic aldol condensation, yield = 96%	141
41	CAUMOF-15	Ba(II)	1D	$[BaO_8]_n$	Ba(4,4′-sulfonyldibenzoic acid$)(DMF)_4$	BaO_8	Monoclinic	$P2_1/n$		Decomposition $T = 400$ °C	142
42	CAUMOF-16	Ba(II)	1D	$[BaO_9]_n$	Ba_2(1,2,4,5-benzenetetracarboxylic acid$)(H_2O)$	BaO_9, BaO_{10}	Monoclinic	$C2/c$		Decomposition $T = 400$ °C	142

Table 1 (*Contd.*)

No.	MOF	Metal	ISBU	ISBU composition	Formula	Coordination polyhedron	Crystallography system	Space group	Topology	Properties & applications	Ref.
43	Fe(II)-MOF-1	Fe(II)	1D	$[FeO_2S_2]_n$	Fe(6-mercaptonicotinic acid)$_2$	FeS_4O_2	Monoclinic	$P2_1/c$		Antiferromagnetic behaviour at 20 K	76
44	Fe(II)-MOF-2	Fe(II)	1D	$[Fe_3(CO_2)_8]_n$	$[NH_2(CH_3)_2][FeII_5(1,3,5\text{-benzenetricarboxylate})_3(Ac)_2(DMA)_2]$	FeO_6	Monoclinic	$P2_1/c$		Antiferromagnetic interaction at 3 K	143
45	MIL-62	Fe(II)	1D	$[FeO_6]_n$	Fe$_2$(2,4,5-benzenetetracarboxylates)	FeO_6	Monoclinic	$C2/m$		Antiferromagnetic below 25 K	144
46	Cd-MOF-1	Cd(II)	1D	$[CdON]_n$	Cd$_2$(BMB)$_{0.5}$(3,3′,5,5′-tetracarboxylate)	$Cd1O_7$, $Cd2O_5N$	Triclinic	$P\bar{1}$		Purple fluorescent	79
47	Cd-MOF-2	Cd(II)	1D	$\{[Cd(COO)]^+\}_n\{[Cd_2(bptc)]^{3+}\}_n$	$[Cd_2(1,4\text{-bis(2-methylbenzimidazol-1-ylmethyl) benzene})_{0.5}(3,3′,4,4′\text{-benzophenonetetracarboxylic acid})]_n$	$Cd1O_5$, $Cd2O_8$	Triclinic	$P\bar{1}$		Decomposition $T = 429$ °C	79
48	Cd-MOF-3	Cd(II)	1D	$[CdO_7]_n$	$[Cd(3,6\text{-di(3-imidazolyl)benzene-1,2-diamine})_{1.5}(5\text{-hydroxyisophthalic acid})]\cdot(H_2O)$	CdO_7	Orthorhombic	$Fdd2$	**hxg-d**		145
49	Cd-MOF-4	Cd(II)	1D	$[Cd_4(CO_2)_8(OH)_2]_n$	$[Cd_2(\text{bis(4-carboxylphenyl)amine})_2(H_2O)]\cdot(H_2O)_2$	$Cd1O_7$, $Cd2O_8$	Triclinic	$P\bar{1}$		Disposition $T = 300$ °C	146
50	Cd-MOF-5	Cd(II)	1D	$[Cd–O–C]_n$	$[Cd(L)_{0.5}(\text{isophthaloylbisglycine})]$	CdO_6	Monoclinic	$C2/c$	**hxg-d**		145
51	Cd-MOF-6	Cd(II)	2D	$[Cd_3(suc)_2]_n$	$[Cd_3(\text{succinate})_{2.5}(4,4′\text{-dipyridylamine})_2](ClO_4)$	$Cd1O_6$, $Cd2N_2O_5$, $Cd3N_2O_5$	Triclinic	$P\bar{1}$			145
52	CdNa-MOF-1	Cd(II)	3D	$[Cd_3(BTC)_4]_n$	$Cd_3Na_6(1,3,5\text{-benzenetricarboxylic})_4(H_2O)_{12}$	$Cd1O_6$, $Cd2O_8$	Tetragonal	$P4_2/n$		H_2 uptake of 1.11 wt% at 77 K	23
53	CAU-46	Ni(II)	1D	$[Ni_2O_{10}]_n$	$[Ni_2(1,1,2,2\text{-tetrakis[4-phosphonophenyl] ethylene})(H_2O)_6]$	NiO_6	Monoclinic	$C2/c$	**pts**	Decomposition $T = 550$ °C	73
54	CAU-47	Co(II)	1D	$[Co_2O_6]_n$	$[Co_2(1,1,2,2\text{-tetrakis[4-phosphonophenyl] ethylene})(H_2O)_4]$	CoO_6	Monoclinic	$C2/c$	**pts**	Decomposition $T = 380$ °C	73
55	Cu-MOF	Cu(II)	1D	$[CuO_6]_n$	$[Cu_4(\mu_3\text{-OH})_4(4,4′\text{-(phenylazanediyl)dibenzoic acid})_2]$	CuO_6	Orthorhombic	$Pnna$		Proton conductivity = 3.98×10^{-6} S cm^{-1}	78
56	USTC-7	Zn(II)	1D	$[ZnO_6]_n$	$Zn_2(4'\text{-(1}H\text{-tetrazol-5-yl)-[1,1′-biphenyl]-3,5-dicarboxylic acid})(\mu_3\text{-OH})(H_2O)_2$	ZnO_6	Orthorhombic	$Cmcm$			147
57	MOF-303	Al(III)	1D	$[Al(–OH)Al]_n$	$Al(OH)(1H\text{-pyrazole-3,5-dicarboxylic})$	AlO_6	Monoclinic	$P2_1/c$	**xhh**	Water uptake of 0.45 g g^{-1} at 25 °C	3
58	CAU-15-Cit	Al(III)	1D	$[AlO_6]_n$	$Al_2(OH)_4(O_2C–C_3H_4–CO_2)$	AlO_6	Monoclinic	$C2/c$		Decomposition $T = 350$ °C	86
59	CAU-8-OBD	Al(III)	1D	$[AlO_6]_n$	$Al(4,4′\text{-oxydibenzoic})_2(OH)$	AlO_6	Tetragonal	$I4_1/a$		CO_2 adsorb = 70 mg g^{-1} at 298 K	84
60	Al-CAU-13	Al(III)	1D	$[AlO_6]_n$	$[Al(OH)(O_2C–C_6H_{10}–CO_2)]\cdot H_2O$	AlO_6	Triclinic	$P\bar{1}$			83
61	CAU-51	Ga(III)	1D	$[GaO_6]_n$	$Ga(OH)(2,5\text{-thiophenedicarboxylic})$	GaO_6	Monoclinic	$P2_1/c$		Water sorption = 370 mg g^{-1} under $p/p_0 = 0.38$	91
62	CAU-43	In(III)	1D	$[InO_6]_n$	$In(OH)[Fe(C_5H_4)_2(COO)_2]$	InO_6	Monoclinic	$C2/c$		Decomposition $T = 250$ °C	93
63	In-MIL-53	In(III)	1D	$[InO_6]_n$	$In(OH)[Fe(C_5H_4)_2(COO)_2]$	InO_6	Monoclinic	$C2/c$		Decomposition $T = 350$ °C	93
64	La,Pr-MOF	Ln(III)	1D	$[LnO_6]_n$	Ln(3,6-di(3-imidazolyl)benzene-1,2-diamine)(DMF)(H_2O)(HCOO),Ln = La,Pr	LnO_6	Monoclinic	$C2/c$			148

Table 1 (*Contd.*)

No.	MOF	Metal	ISBU	ISBU composition	Formula	Coordination polyhedron	Crystallography system	Space group	Topology	Properties & applications	Ref.
65	Ln-MOF	Ln(III)	1D	$[Ln_2O_{17}]_n$	$Ln_2(Succ)_3(H_2O)_2$, Ln = La, Pr, Nd, Sm, Eu, Gd and Tb	$Ln2O_{17}$	Triclinic	$P\bar{1}$	**pcu**		149
66	CAU-35	Bi(III)	1D	$[BiO]_n$	$Bi_2(O)(OH)$(1,3,5-triazine-2,4,6-tribenzoate)	$Bi1O_7$, $Bi2O_7$	Orthorhombic	$Pna2_1$			96
67	CAU-50	Sc(III)	1D	$[ScO_6]_n$	Sc_2(1,1′-ferrocenedicarboxlic)$_3$	ScO_6	Orthorhombic	*Pnna*		Decomposition $T = 250$ °C	99
68	MFM-300	Cr(III)	1D	$[CrO_4(OH)_2]_n$	$Cr_2(OH)_2$(biphenyl-3,3′,5,5′-tetracarboxylic)	CrO_6	Tetragonal	$I4_122$		SO_2 uptake up to 8.59 mmol g^{-1} at 273 K	31
69	CTH-16	Gd(III)	1D	$[GdO_9]_n$	Gd_2(Benzene-1,2,4,5-tetracarboxylate)$_2$	GdO_9	Triclinic	$P\bar{1}$	**htp**	Decomposition $T = 350$ °C	21
70	CTH-15	Ce(III)	2D	$[CeO]_n$	Ce_3(Benzene-1,2,4,5-tetracarboxylate)(benzene-1,2,4,5-tetracarboxylate acid)(OAc)(HCO_2)	Ce1–O, Ce2–O,Ce3–O	Monoclinic	$P2_1/c$		Decomposition $T = 350$ °C	21
71	Ce(III)-MOF	Ce(III)	1D	$[CeO_9]_n$	$[Ce_2$(3,6-Di(3-imidazolyl)benzene-1,2-diamine$)_3(DMA)_3(H_2O)_4]_n$ DMA	CeO_9	Triclinic	$P\bar{1}$	**sql**		148
72	Tb-MOF	Tb(III)	1D	$[TbO_9]_n$	[Tb(3,6-di(3-imidazolyl)benzene-1,2-diamine$)(DMA)_2(NO_3)]_nH_2O$	TbO_9	Triclinic	$P\bar{1}$			148
73	La -MOF	La(III)	1D	$[LaO_{11}]_n$	$[La_2(Succ)_3(H_2O)_3]\cdot 2H_2O$	LaO_{11}	Orthorhombic	*Pbnm*	**pcu**	Decomposition $T = 420$ °C	150
74	MIL-177-HT	Ti(IV)	1D	$[Ti_6O_9]_n$	$Ti_{12}O_{15}$(5,5′-methylenediisophthalic$)_3$(formate$)_6$	TiO_6	Hexagonal	*P6/mmm*		Photocarrier mobility = 4×10^{-4} cm^2 s^{-1} V^{-1}	27
75	ZSTU-1	Ti(IV)	1D	$[Ti(\mu_3\text{-}O)_6(\mu_3\text{-}OH)_6(COO)_6]_n$	$Ti_6(\mu_3\text{-}O)_6(\mu_2\text{-}OH)_6$(4,4′,4″-nitrilotribenzoic$)_2(H_2O)(DMF)_2$	$Ti_6(\mu_3\text{-}O)_6(COO)_6$	Hexagonal	$P6_3/mcm$	**kgd**	Hydrogen evolution rate: 1120 μmol g^{-1} h^{-1}	18
76	ZSTU-2	Ti(IV)	1D	$[Ti(\mu_3\text{-}O)_6(\mu_3\text{-}OH)_6(COO)_6]_n$	$Ti_6(\mu_3\text{-}O)_6(\mu_2\text{-}OH)_6$(1,3,5-tris(4-carboxyphenyl) benzene$)_2(H_2O)$	$Ti_6(\mu_3\text{-}O)_6(COO)_6$	Hexagonal	$P6_3/mcm$		Hydrogen evolution rate: 390 μmol g^{-1} h^{-1}	18
77	ZSTU-3	Ti(IV)	1D	$[Ti(\mu_3\text{-}O)_6(\mu_3\text{-}OH)_6(COO)_6]_n$	$Ti_6(\mu_3\text{-}O)_6(\mu_2\text{-}OH)_6$(tris(4′-carboxybiphenyl) amine$)_2(H_2O)(DMF)_2$	$Ti_6(\mu_3\text{-}O)_6(COO)_6$	Hexagonal	$P6_3/mcm$		Hydrogen evolution rate: 1350 μmol g^{-1} h^{-1}	18
78	COK-47	Ti(IV)	2D	$[TiO_6]_n$	Cp_2TiCl_2	TiO_6	Triclinic	$P\bar{1}$		Photocatalytic dibenzothiophene oxidation (Con. = 99%)	19
79	CAU-22	Zr(IV)	1D	$[Zr_6O_4(OH)_4(\mu_2\text{-}OH)_2]_n$	$Zr_6(\mu_3\text{-}O)_4(\mu_3\text{-}OH)_4(\mu_2\text{-}OH)_2$(1*H*-pyrazole-3,5-dicarboxylic$)_3(OH)_2(H_2O)_2(HCO_2)_2$	$Zr_6O_4(OH)_4$	Monoclinic	*C2/m*		Decomposition $T = 270$ °C	38
80	CAU-27	Zr(IV)	1D	$[Zr_6O_4(OH)_4]_n$	$[Zr_5O_4(OH)_4(OAc)_4(BDC)_2]$	$Zr_6O_4(OH)_4$	Tetragonal	I_4/mcm		Decomposition $T = 470$ °C	17
81	MIL-163	Zr(IV)	1D	$[ZrO_8]_n$	[Zr(H_2-TzGal)]	ZrO_8	Tetragonal	$P4_2/mmc$		CO_2 uptake (6 mmol g^{-1}) at 298 K and 25 bar	106
82	ZrPP-1	Zr(IV)	1D	$[ZrO_8]_n$	Zr_2(THPP)	ZrO_8	Tetragonal	$P4_2/mmc$	**nbo**	CO_2 uptake = 87.7 cm^3 g^{-1} at 273K, CO production rate = 210 μmol g^{-1}	34
83	Zr-MIL-140-4F	Zr(IV)	1D	$[ZrO_7]_n$	[ZrO(BDC-F_4)]	ZrO_7	Monoclinic	$C2_1/c$		C_2H_2/CO_2 separation, Sel. = 2.7	30
84	PCN-226	Zr(IV)	1D	$[ZrO_7]_n$	Zr_3O_3(Tetrakis(4-carboxyphenyl) porphyrin)(benzoate$)_2$	ZrO_7	Orthorhombic	*Ibam*	**ztt**	Zn–air battery with specific capacity up to 724 mA h g^{-1}	32
85	Ce-MIL-140-4F	Ce(IV)	1D	$[CeO_7]_n$	[CeO(BDC-F_4)]	CeO_7	Monoclinic	$C2_1/c$		CO_2/C_2H_2 separation, Sel. = 2.5	30
86	NSM	Np(V)	1D	$[NpO_7]_n$	$[(CH_3)_2NH_2]_4[(NpO_2)_4(C_{53}O_8H_{32})(HCOO)_4]$	NpO_7	Tetragonal	$I4_1/a$			16

Moreover, Alshareef and his colleagues[35] applied the 1D titanium-phosphonate MOF-based nanowires (TiPNW) for photocatalytic water splitting. Under light irradiation, the photoexcited electrons were transferred from organophosphorus linkers to 1D Ti-oxo chains *via* an efficient linker-to-metal node charge transfer (LCMT) path. With the aid of co-catalytic Pt NPs, electrons were further separated from the resulting Ti^{3+} intermediates and utilized for the reduction of water. Meanwhile, concurrent holes were located at the organic linker and quenched by TEOA. As shown in Fig. 25e, TiPNW with a rationally designed linker showed the highest photocatalytic hydrogen evolution rate up to 1260 μmol h^{-1} g^{-1}, nearly five times the rate of commercial anatase.

The dense spatial packing of active sites among ISBU MOFs is anticipated for the activation of substrate cooperatively in catalysis.[32,34] In 2018, Lin *et al.*[34] constructed a series of 1D phenolic porphyrinc ZrPP-1-M (M = Co, Fe, Cu, Zn, H_2) for selective photoreduction of CO_2 to CO. According to the CO_2 adsorption isotherms (Fig. 26a), ZrPP-1-M (M = Co, Fe, Cu, Zn, H_2) have presented high CO_2 uptake of 87.7 88.4, 59.8, 77.5, 81.9 cm^3 g^{-1}, respectively, at 273 K. Such small adsorption disparency was ascribed to the atomic mass of installed metal types rather than their CO_2 adsorption strength, as verified by their nearly identical isosteric heats. It was suggested that the strong CO_2 adsorption among ZrPP-1-M resulted from the densely eclipsed stacking of parallel metalloporphyrins enforced by its unique 1D Zr-oxo chain, which anchored two oxygens of CO_2 molecule *via* a pair of positively charged metal centers. Bearing this in mind, ZrPP-1-M was further tested in the photoreduction of CO_2. ZrPP-1-Co with the narrowest band gap capable of efficient visible light absorption showed the highest CO production rate among tested samples (Fig. 26b).

By taking the robustness advantages, moreover, Bueken *et al.*[19] successfully introduced substantial defects into 2D COK-47s for photooxidation of dibenzothiophene (DBT). It was found that there were two-fold functions of the introduced linker-missing defects in the catalysis. First, the pore size of COK-47s was enlarged to 6 Å (Fig. 26c) by missing organic linkers, which was favorable for substrate diffusion. Second, the open Ti sites as catalytical Lewis acids were competent for efficient substrate activations. Experiment results showed that COK-47s indeed exerted the highest conversion rate among all tested samples including the defect-free COK-47_L reference, familiar Ti-MOFs, Zr-MOFs and commercial P25 TiO_2 (Fig. 26d). Furthermore, the robust 2D inorganic sheet structure of COK-47s has taken charge of its stable catalytic performance within three cycling tests, which was keen merit rarely reported in the defect-based catalysts.

4. Conclusion and outlook

In this review, we have thoroughly introduced the recent development of MOFs of infinite secondary building units (ISBUs) including 1D chains, 2D sheets and 3D nets. On account of the unique inorganic nature resembling metal-oxides/hydroxides, ISBU MOFs have been conferred ultrahigh packing density of building blocks, robust physical/chemical stabilities, superior semiconductor-like conductivity and carrier mobility, and so on. Therefore, a blooming growth of applications of ISBU MOFs has been made in the fields of gas adsorption, gas separation, energy storage and catalysis. We have also summarized the prototypes and recently developed examples of ISBU MOFs for easy reference and direct comparison (Table 1).

While, ISBU MOFs also have some disadvantages in comparison to conventional discrete node MOFs. Up till now, the development of ISBU MOFs is still in its infancy and most of the examples have been obtained by trial and error, without guidable principles and universe protocols. In spite of the robust stabilities, the formation of dense ISBU at certain dimensions somewhat decreases porosities and specific surface areas of resultant MOFs. Equally, it is more or less difficult to functionalize corresponding MOFs *via* modifying the pure inorganic ISBUs. Challenges are always with opportunities. Hence, some perspectives are also provided according to our personal insights.

(1) It is well known that reticular chemistry[151,152] guided the structure design and deciphering of MOFs in virtue of topology. Unfortunately, the dense and complicated metal-oxo interconnection casts hardly unified standards for the topological decomposition of ISBU MOFs. Taking a scenario, the usually adopted "all-nodes" and "extension-of-points" approaches face troubles in connecting the simplified nodes of ISBU MOFs, which is totally different from the case of OD metal nodes only connected by organic edges. As a result, how to construct ISBU MOFs with ordered and well-defined structures and topologies is still an open question. Considering the pure inorganic ISBU nature resembling traditional metal oxides and metal hydroxides, we suggest that a fundamental crystallographic and property understanding of those inorganics might be essential for further development of ISBU MOFs with well-defined compositions and structures. As a proof-of-concept, the very recently reported metal hydroxide-organic frameworks[153] have been successfully obtained from corresponding hydroxide precursors.

(2) Hydrothermal and solvothermal strategies are routinely utilized for the synthesis of various types of MOFs witnessed with great success in past decades. With regard to ISBU MOFs, the metal-oxo inorganic nature renders them forming corresponding metal-oxide/hydroxides byproduct easily in conventional solvent-involved conditions. Especially for alkali metal cations (*e.g.* Li^+, Na^+ and K^+), the strong solvation effect results in an overwhelming competition with the organic linker coordination, and hence usual formations of unstable frameworks with excessive adsorbed solvents. Mechano-assisted syntheses like grinding and balling free of solvent are suggested as potential workable routes.

(3) Single-crystal X-ray diffraction (SCXRD) is widely accepted as the golden tool for characterization of emerged novel MOFs. However, powdery polycrystals with micrometer scales are insufficient for SCXRD characterization but are popularly obtained in examples of ISBU MOFs. Aims at obtaining accurate crystallographic information, low-dose transmission electron/high-resolution cryo-electron microscopy, continuous 3D

electron diffraction together with theoretic modeling are suggested as the combinational standard.

(4) Though unique physical/chemical properties stemming from their inorganic character, the application scopes of ISBU MOFs are still very limited. In addition to achievements in adsorption, gas separation, energy storage and photocatalysis, opto- and electro-devices based on ISBU MOFs by fully exploiting their inorganic semiconductor-like and flexible organic characters are very appealing but still are virgin research fields. Besides, ISBU MOFs may become a very potential bridge across inorganic chemistry and biomaterials *via* selections of low toxic (*e.g.*, alkali and alkali earth) metal-oxo building blocks and biocompatible organic linkers (*e.g.*, amino acid and peptide derivates). For instance, chiral ISBU MOFs designed for drug loading, anti-tumor and/or bioimaging are welcome.

(5) Equally importantly, the fundamental mechanism study is essential to pursue better performances as well as expand application scope *via* the made-to-order structure redesign. Hence, much more effort attempting to in-depth understand the ISBU functions by the time-resolved and operando technologies is highly desirable to be devoted.

In spite of the standing challenges, the unique structure character and associated intriguing physicochemical properties of ISBU MOFs will attract much more effort devoted to this emerging research field. We can foresee that much more novel ISBU MOFs will be rationally designed, controllably synthesized and competently applied in versatile fields in the near future.

Abbreviations

L1	4,4′,4″-(Methylsilanetriyl)tribenzoate
L2	4,4′,4″,4‴-Silanetetrayltetrabenzoate
L3	1,4-Bis(phenylthio)but-2-yne
H_2L4	3,3′-Dihydroxy-[1,1′-biphenyl]-4,4′-dicarboxylic acid
L5	1,3,5-Tri(2-carboxymethyltetrazol-5-yl)benzene
L6	3,3′,5,5′-Biphentetrolate
H_4L7	Biphenyl-3,3′,5,5′-tetracarboxylic acid
4,4-BPDC	4,4-Bisphthalboxylate
6-H_2MNA	6-Mercaptonicotinic acid
BDA	(2*S*, 2′*S*)-2,2′-(Terephthaloylbis(azanediyl)) disuccinate
BDC	1,4-Benzenedicarboxylate
BMB	1,4-Bis(2-methylbenzimidazol-1-methylmethyl) benzene
BPDA	(2*S*,2′*S*)-2,2′-(([1,1′-Biphenyl]-4,4′-dicarbonyl) bis(azanediyl)) di-succinate
BPTC	1,1′-Biphenyl-2,2′,6,6′-tetracarboxylate
BTB	1,3,5-Tris(4-carboxyphenyl)benzene
CB	Conduction band
Cp	Cyclopentadienyl
dach	*trans*-1,2-Diaminocyclohexane
DOBPTC	4,4′-Di-oxidobiphenyl-3,3′-dicarboxylate
DFT	Density functional theory
DMF	*N*,*N*-Dimethylformamide
FP-TRMC	Flash photoluminescence time-resolved microwave conductivity
H_4BPTC	3,3′,4,4′-Benzophenone tetracarboxylic acid
H_3BTC	1,3,5-Benzenetricarboxylic acid
H_3BTCA	Tris(4′-carboxybiphenyl)amine acid
H_4BTEC	Benzene-1,2,4,5-tetracarboxylate acid
HER	Hydrogen evolution reaction
H_2FcDC	1,1′-Ferrocenedicarboxlic acid
H_2FDC	Furan-2,4-dicarboxylic acid
H_4MDIP	5,5′-Methylenediisophthalic acid
H_2OBD	4,4′-Oxydibenzoic acid
H_2PZDC	1*H*-Pyrazole-3,5-dicarboxylic acid
H_3TCA	4,4′,4″-Nitrilotribenzoic acid
H_2TCPP	Tetrakis(4-carboxyphenyl)porphyrin acid
H_2TDC	2,5-Thiophenedicarboxylic acid
H_2TFBDC	Tetrafluoro-terephthalic acid
H_4(TTF-TC)	Tetrathiafulvalene tetracarboxylic acid
H_6TzGal	5,5′-(1,2,4,5-Tetrazine-3,6-diyl)bis(benzene-1,2,3-triol) acid
IAST	Ideal adsorbed solution theory
IPr	Isopropoxide
LCCT	Linker-to-cluster charge transfer
LMCT	Ligand-to-metal charge transfer
NH_2–H_2BDC	2-Amino-1,4-benzenedicarboxylic acid
NDC	2,6-Naphathalenedicarboxylate
OER	Oxygen-evolution reaction
ORR	Oxygen-involved reduction
PDC	3,5-Pyridinedicarboxylate
TATB	1,3,5-Triazine-2,4,6-tribenzoate
TEOA	Triethanolamine
THPP	5,10,15,20-Tetrakis(3,4,5-trihydroxyphenyl) porphyrin
TiPNW	Titanium-phosphonate MOF based nanowires
TTC	Trithiocyanuric acid
UL	Ultralight

Conflicts of interest

There are no conflicts to declare.

Acknowledgements

This work is supported by National Natural Science Foundation of China (No. 22103055, 21905195 and 22073070), Natural Science Foundation of Tianjin City (No. 20JCYBJC00800), Science and Technology Plans of Tianjin (21ZYJDJC00050) and PEIYANG Young Scholars Program of Tianjin University (No. 2020XRX-0023).

Notes and references

1 W. Cheng, H. Zhang, D. Luan and X. W. D. Lou, *Sci. Adv.*, 2021, **7**, eabg2580.
2 Y. Zhang, J. Guo, J. Zhang, X. Qiu, X. Zhang, J. Han, B. Zhang, C. Long, Y. Shi, Z. Yang, W. Zhao and Z. Tang, *Chem*, 2022, **8**, 1688–1704.
3 N. Hanikel, X. Pei, S. Chheda, H. Lyu, W. Jeong, J. Sauer, L. Gagliardi and O. M. Yaghi, *Science*, 2021, **374**, 454–459.

4 M. Zhao, K. Yuan, Y. Wang, G. Li, J. Guo, L. Gu, W. Hu, H. Zhao and Z. Tang, *Nature*, 2016, **539**, 76–80.
5 L. Wang, H. Xu, J. Gao, J. Yao and Q. Zhang, *Coord. Chem. Rev.*, 2019, **398**, 213016.
6 J. Guo, Y. Qin, Y. Zhu, X. Zhang, C. Long, M. Zhao and Z. Tang, *Chem. Soc. Rev.*, 2021, **50**, 5366–5396.
7 M. J. Kalmutzki, N. Hanikel and O. M. Yaghi, *Sci. Adv.*, 2018, **4**, eaat9180.
8 J. Guo, Y. Zhang, Y. Zhu, C. Long, M. Zhao, M. He, X. Zhang, J. Lv, B. Han and Z. Tang, *Angew. Chem., Int. Ed.*, 2018, **57**, 6873–6877.
9 Z. H. Syed, F. Sha, X. Zhang, D. M. Kaphan, M. Delferro and O. K. Farha, *ACS Catal.*, 2020, **10**, 11556–11566.
10 H. Deng, S. Grunder, K. E. Cordova, C. Valente, H. Furukawa, M. Hmadeh, F. Gandara, A. C. Whalley, Z. Liu, S. Asahina, H. Kazumori, M. O'Keeffe, O. Terasaki, J. F. Stoddart and O. M. Yaghi, *Science*, 2012, **336**, 1018–1023.
11 X. Zhang, Z. Chen, X. Liu, S. L. Hanna, X. Wang, R. Taheri Ledari, A. Maleki, P. Li and O. K. Farha, *Chem. Soc. Rev.*, 2020, **49**, 7406–7427.
12 Y. Bai, Y. Dou, L. H. Xie, W. Rutledge, J. R. Li and H. C. Zhou, *Chem. Soc. Rev.*, 2016, **45**, 2327–2367.
13 M. J. Kalmutzki, N. Hanikel and O. M. Yaghi, *Sci. Adv.*, 2018, **4**, eaat9180.
14 W. Xu, B. Tu, Q. Liu, Y. Shu, C. Liang, C. S. Diercks, O. M. Yaghi, Y. Zhang, H. Deng and Q. Li, *Nat. Rev. Mater.*, 2020, **5**, 764–779.
15 H. Zhou, J. R. Long and O. M. Yaghi, *Chem. Rev.*, 2012, **112**, 673–674.
16 S. E. Gilson, M. Fairley, S. L. Hanna, J. E. S. Szymanowski, P. Julien, Z. Chen, O. K. Farha, J. A. LaVerne and P. C. Burns, *J. Am. Chem. Soc.*, 2021, **143**, 17354–17359.
17 S. Leubner, H. Zhao, N. Van Velthoven, M. Henrion, H. Reinsch, D. E. De Vos, U. Kolb and N. Stock, *Angew. Chem., Int. Ed.*, 2019, **58**, 10995–11000.
18 C. Li, H. Xu, J. Gao, W. Du, L. Shangguan, X. Zhang, R.-B. Lin, H. Wu, W. Zhou, X. Liu, J. Yao and B. Chen, *J. Mater. Chem. A*, 2019, **7**, 11928–11933.
19 S. Smolders, T. Willhammar, A. Krajnc, K. Sentosun, M. T. Wharmby, K. A. Lomachenko, S. Bals, G. Mali, M. B. J. Roeffaers, D. E. De Vos and B. Bueken, *Angew. Chem., Int. Ed.*, 2019, **58**, 9160–9165.
20 H. Jia, Q. Han, W. Luo, H. Cong and H. Deng, *Chem. Catal.*, 2022, **2**, 84–101.
21 F. M. Amombo Noa, M. Abrahamsson, E. Ahlberg, O. Cheung, C. R. Göb, C. J. McKenzie and L. Öhrström, *Chem*, 2021, **7**, 2491–2512.
22 Y. Kamakura, P. Chinapang, S. Masaoka, A. Saeki, K. Ogasawara, S. R. Nishitani, H. Yoshikawa, T. Katayama, N. Tamai, K. Sugimoto and D. Tanaka, *J. Am. Chem. Soc.*, 2020, **142**, 27–32.
23 Y. Fu, J. Su, Z. Zou, S. Yang, G. Li, F. Liao and J. Lin, *Cryst. Growth Des.*, 2011, **11**, 3529–3535.
24 M. K. Kim and K. M. Ok, *CrystEngComm*, 2011, **13**, 4599–4603.
25 N. Kolobov, M. G. Goesten and J. Gascon, *Angew. Chem., Int. Ed.*, 2021, **60**, 26038–26052.
26 D. Banerjee, S. J. Kim and J. B. Parise, *Cryst. Growth Des.*, 2009, **9**, 2500–2503.
27 S. Wang, T. Kitao, N. Guillou, M. Wahiduzzaman, C. Martineau Corcos, F. Nouar, A. Tissot, L. Binet, N. Ramsahye, S. Devautour Vinot, S. Kitagawa, S. Seki, Y. Tsutsui, V. Briois, N. Steunou, G. Maurin, T. Uemura and C. Serre, *Nat. Commun.*, 2018, **9**, 1660–1668.
28 J. D. Martell, L. B. Porter Zasada, A. C. Forse, R. L. Siegelman, M. I. Gonzalez, J. Oktawiec, T. e. Runčevski, J. Xu, M. Srebro Hooper, P. J. Milner, A. Colwell, J. Autschbach, J. A. Reimer and J. R. Long, *J. Am. Chem. Soc.*, 2017, **139**, 16000–16012.
29 F. Fathieh, M. J. Kalmutzki, E. A. Kapustin, P. J. Waller, J. Yang and O. M. Yaghi, *Sci. Adv.*, 2018, **4**, eaat3198.
30 Z. Zhang, S. B. Peh, R. Krishna, C. Kang, K. Chai, Y. Wang, D. Shi and D. Zhao, *Angew. Chem., Int. Ed.*, 2021, **60**, 17198–17204.
31 L. Briggs, R. Newby, X. Han, C. G. Morris, M. Savage, C. P. Krap, T. L. Easun, M. D. Frogley, G. Cinque, C. A. Murray, C. C. Tang, J. Sun, S. Yang and M. Schröder, *J. Mater. Chem. A*, 2021, **9**, 7190–7197.
32 M. O. Cichocka, Z. Liang, D. Feng, S. Back, S. Siahrostami, X. Wang, L. Samperisi, Y. Sun, H. Xu, N. Hedin, H. Zheng, X. Zou, H. C. Zhou and Z. Huang, *J. Am. Chem. Soc.*, 2020, **142**, 15386–15395.
33 Y. Pan, Q. Li, H. Li, J. Farmakes, A. Ugrinov, X. Zhu, Z. Lai, B. Chen and Z. Yang, *Chem. Catal.*, 2021, **1**, 146–161.
34 E. X. Chen, M. Qiu, Y. F. Zhang, Y. S. Zhu, L. Y. Liu, Y. Y. Sun, X. Bu, J. Zhang and Q. Lin, *Adv. Mater.*, 2018, **30**, 1704388–1704395.
35 Y. P. Zhu, J. Yin, E. Abou Hamad, X. Liu, W. Chen, T. Yao, O. F. Mohammed and H. N. Alshareef, *Adv. Mater.*, 2020, **32**, 1906368–1906375.
36 Y. Keum, S. Park, Y. P. Chen and J. Park, *Angew. Chem., Int. Ed.*, 2018, **57**, 14852–14856.
37 A. Cadiau, N. Kolobov, S. Srinivasan, M. G. Goesten, H. Haspel, A. V. Bavykina, M. R. Tchalala, P. Maity, A. Goryachev, A. S. Poryvaev, M. Eddaoudi, M. V. Fedin, O. F. Mohammed and J. Gascon, *Angew. Chem., Int. Ed.*, 2020, **59**, 13468–13472.
38 S. Waitschat, H. Reinsch and N. Stock, *Chem. Commun.*, 2016, **52**, 12698–12701.
39 H. Putz and K. Brandenburg, *Crystal Impact-GbR*, Kreuzherrenstr, 2006, vol. 102, p. 53227.
40 K. Momma and F. Izumi, *J. Appl. Crystallogr.*, 2011, **44**, 1272–1276.
41 A. Schoedel, M. Li, D. Li, M. O'Keeffe and O. M. Yaghi, *Chem. Rev.*, 2016, **116**, 12466–12535.
42 D. Pugh, E. Ashworth, K. Robertson, L. C. Delmas, A. J. P. White, P. N. Horton, G. J. Tizzard, S. J. Coles, P. D. Lickiss and R. P. Davies, *Cryst. Growth Des.*, 2018, **19**, 487–497.
43 D. Banerjee, L. A. Borkowski, S. J. Kim and J. B. Parise, *Cryst. Growth Des.*, 2009, **9**, 4922–4926.

44 A. Nguyen Tle, R. Demir Cakan, T. Devic, M. Morcrette, T. Ahnfeldt, P. Auban Senzier, N. Stock, A. M. Goncalves, Y. Filinchuk, J. M. Tarascon and G. Ferey, *Inorg. Chem.*, 2010, **49**, 7135–7143.
45 P. Siman, C. A. Trickett, H. Furukawa and O. M. Yaghi, *Chem. Commun.*, 2015, **51**, 17463–17466.
46 X. Zhao, M. S. Shimazu, X. Chen, X. Bu and P. Feng, *Angew. Chem., Int. Ed.*, 2018, **57**, 6208–6211.
47 J. H. Lee, B. Moon, T. K. Kim, S. Jeoung and H. R. Moon, *Dalton Trans.*, 2015, **44**, 15130–15134.
48 S. Q. Bai, I. H. K. Wong, N. Zhang, K. Lin Ke, M. Lin, D. J. Young and T. S. A. Hor, *Dalton Trans.*, 2018, **47**, 16292–16298.
49 F. Liu, P. Hao, T. Yu, Q. Guan and Y. Fu, *J. Mol. Struct.*, 2016, **1119**, 431–436.
50 S. Q. Bai, J. Y. Kwang, L. L. Koh, D. J. Young and T. S. Hor, *Dalton Trans.*, 2010, **39**, 2631–2636.
51 Q. Lin, T. Wu, S. T. Zheng, X. Bu and P. Feng, *Chem. Commun.*, 2011, **47**, 11852–11854.
52 R. K. Vakiti, B. D. Garabato, N. P. Schieber, M. J. Rucks, Y. Cao, C. Webb, J. B. Maddox, A. Celestian, W.-P. Pan and B. Yan, *Cryst. Growth Des.*, 2012, **12**, 3937–3943.
53 D. Briones, P. Leo, J. Cepeda, G. Orcajo, G. Calleja, R. Sanz, A. Rodríguez-Diéguez and F. Martínez, *CrystEngComm*, 2018, **20**, 4793–4803.
54 K. S. Asha, M. Makkitaya, A. Sirohi, L. Yadav, G. Sheet and S. Mandal, *CrystEngComm*, 2016, **18**, 1046–1053.
55 X. Chen, A. M. Plonka, D. Banerjee and J. B. Parise, *Cryst. Growth Des.*, 2012, **13**, 326–332.
56 R. K. Birkedal Nielsen, K. O. Kongshaug and H. Fjellvåg, *Solid State Sci.*, 2006, **8**, 1237–1242.
57 D. Guo, C. M. Liang, K. Chiu and W. K. Wang, *Z. Anorg. Allg. Chem.*, 2021, **647**, 1193–1197.
58 J. Yang, S. Zhang, Z. Feng, Y. Cao and D. R. Zhu, *Dalton Trans.*, 2021, **50**, 11975–11985.
59 F. Dai, X. Wang, Y. Wang, Z. Liu and D. Sun, *Angew. Chem., Int. Ed.*, 2020, **59**, 22372–22377.
60 Y. Sun, B.-X. Dong and W.-L. Liu, *J. Solid State Chem.*, 2019, **278**, 120897–120903.
61 W. z. Zhang, T. y. Lv, D. z. Wei, R. Xu, G. Xiong, Y. q. Wang, E. j. Gao and Y. g. Sun, *Inorg. Chem. Commun.*, 2011, **14**, 1245–1249.
62 P. Wang, G. Wu and X. Wang, *J. Inorg. Organomet. Polym. Mater.*, 2012, **22**, 1377–1383.
63 D. Saha, T. Maity, R. Sen and S. Koner, *Polyhedron*, 2012, **43**, 63–70.
64 T. T. Li, S. L. Cai, R. H. Zeng and S. R. Zheng, *Inorg. Chem. Commun.*, 2014, **48**, 40–43.
65 S. Du, C. Ji, X. Xin, M. Zhuang, X. Yu, J. Lu, Y. Lu and D. Sun, *J. Mol. Struct.*, 2017, **1130**, 565–572.
66 C. Volkringer, J. Marrot, G. Férey and T. Loiseau, *Cryst. Growth Des.*, 2008, **8**, 685–689.
67 J. J. Niu, C. Chen, C. W. Ye, X. Zhang, Y. G. Yao and L. F. Chen, *Inorg. Chem. Commun.*, 2013, **27**, 149–151.
68 X. Chen, S. He, F. Chen and Y. Feng, *CrystEngComm*, 2014, **16**, 8706–8709.
69 D. T. Tran, D. Chu, A. G. Oliver and S. R. J. Oliver, *Inorg. Chem. Commun.*, 2009, **12**, 351–354.
70 X. Zhang, Y. Y. Huang, M. J. Zhang, J. Zhang and Y. G. Yao, *Cryst. Growth Des.*, 2012, **12**, 3231–3238.
71 J. A. Rood, B. C. Noll and K. W. Henderson, *Inorg. Chem.*, 2006, **45**, 5521–5528.
72 D. W. Lee, V. Jo and K. M. Ok, *Cryst. Growth Des.*, 2011, **11**, 2698–2701.
73 S. Wohlbrandt, C. Meier, H. Reinsch, E. Svensson Grape, A. K. Inge and N. Stock, *Inorg. Chem.*, 2020, **59**, 13343–13352.
74 A. K. Singh, G. Pandey, K. Singh, A. Kumar, M. Trivedi and V. Singh, *Dalton Trans.*, 2018, **47**, 6386–6393.
75 X. Y. Li, Y. L. Wang, Z. Xue, S. D. Han, Z. Z. Xue and J. Pan, *Cryst. Growth Des.*, 2021, **21**, 5261–5267.
76 S. Du, M. Cui and Z. He, *Inorg. Chem.*, 2021, **60**, 19053–19061.
77 J. Chen, X. Mu, M. Du and Y. Lou, *Inorg. Chem. Commun.*, 2017, **84**, 241–245.
78 B. Ay, O. Şahin and E. Yildiz, *Solid State Sci.*, 2019, **96**, 105958–105966.
79 C. Xu, B. M. Ji, S. B. Miao, D. S. Deng, H. w. Hou and M. h. Li, *Polyhedron*, 2017, **130**, 160–164.
80 Q. Z. Sun, Y. B. Yin, L. Y. Chai, H. Liu, P. F. Hao, X. P. Yan and Y. Q. Guo, *J. Mol. Struct.*, 2014, **1070**, 75–79.
81 M. Wahiduzzaman, D. Lenzen, G. Maurin, N. Stock and M. T. Wharmby, *Eur. J. Inorg. Chem.*, 2018, **2018**, 3626–3632.
82 H. Reinsch, S. Waitschat and N. Stock, *Dalton Trans.*, 2013, **42**, 4840–4847.
83 H. Reinsch, J. Benecke, M. Etter, N. Heidenreich and N. Stock, *Dalton Trans.*, 2017, **46**, 1397–1405.
84 M. Kruger, A. K. Inge, H. Reinsch, Y. H. Li, M. Wahiduzzaman, C. H. Lin, S. L. Wang, G. Maurin and N. Stock, *Inorg. Chem.*, 2017, **56**, 5851–5862.
85 N. Hermer, M. T. Wharmby and N. Stock, *Z. Anorg. Allg. Chem.*, 2017, **643**, 137–140.
86 N. Heidenreich, A. Lieb, N. Stock and H. Reinsch, *Dalton Trans.*, 2018, **47**, 215–223.
87 E. Alvarez, N. Guillou, C. Martineau, B. Bueken, B. Van de Voorde, C. Le Guillouzer, P. Fabry, F. Nouar, F. Taulelle, D. de Vos, J. S. Chang, K. H. Cho, N. Ramsahye, T. Devic, M. Daturi, G. Maurin and C. Serre, *Angew. Chem., Int. Ed.*, 2015, **54**, 3664–3668.
88 C. Volkringer, T. Loiseau, M. Haouas, F. Taulelle, D. Popov, M. Burghammer, C. Riekel, C. Zlotea, F. Cuevas, M. Latroche, D. Phanon, C. Knöfelv, P. L. Llewellyn and G. Férey, *Chem. Mater.*, 2009, **21**, 5783–5791.
89 C. Hao, H. Ren, H. Zhu, Y. Chi, W. Zhao, X. Liu, W. J. S. Guo and P. Technology, *Sep. Purif. Technol.*, 2022, **290**, 120804.
90 R. Hajjar, C. Volkringer, T. Loiseau, N. Guillou, J. Marrot, G. Férey, I. Margiolaki, G. Fink, C. Morais and F. Taulelle, *Chem. Mater.*, 2010, **23**, 39–47.
91 T. Rabe, E. S. Grape, H. Rohr, H. Reinsch, S. Wohlbrandt, A. Lieb, A. K. Inge and N. Stock, *Inorg. Chem.*, 2021, **60**, 8861–8869.
92 S. Hou, X. Zhang, W. Yuan, Y. Li and Z. Gu, *Inorg. Chem.*, 2020, **59**, 11298–11304.

93 J. Benecke, E. S. Grape, A. Fuss, S. Wohlbrandt, T. A. Engesser, A. K. Inge, N. Stock and H. Reinsch, *Inorg. Chem.*, 2020, **59**, 9969–9978.
94 R. J. Li, M. Li, X. P. Zhou, D. Li and M. O'Keeffe, *Chem. Commun.*, 2014, **50**, 4047–4049.
95 M. Köppen, V. Meyer, J. Ångström, A. K. Inge and N. Stock, *Cryst. Growth Des.*, 2018, **18**, 4060–4067.
96 M. Koppen, O. Beyer, S. Wuttke, U. Luning and N. Stock, *Dalton Trans.*, 2017, **46**, 8658–8663.
97 P. Rönfeldt, H. Reinsch, M. P. M. Poschmann, H. Terraschke and N. Stock, *Cryst. Growth Des.*, 2020, **20**, 4686–4694.
98 P. Rönfeldt, H. Reinsch, N. Faßheber, H. Terraschke and N. Stock, *Eur. J. Inorg. Chem.*, 2020, **2020**, 1147–1152.
99 J. Benecke, E. Svensson Grape, T. A. Engesser, A. K. Inge and H. Reinsch, *CrystEngComm*, 2020, **22**, 5569–5572.
100 P. L. Llewellyn, P. Horcajada, G. Maurin, T. Devic, N. Rosenbach, S. Bourrelly, C. Serre, D. Vincent, S. Loera-Serna, Y. Filinchuk and G. Férey, *J. Am. Chem. Soc.*, 2009, **131**, 13002–13008.
101 Y. Yan, C. Li, Y. Wu, J. Gao and Q. Zhang, *J. Mater. Chem. A*, 2020, **8**, 15245–15270.
102 V. Benoit, R. S. Pillai, A. Orsi, P. Normand, H. Jobic, F. Nouar, P. Billemont, E. Bloch, S. Bourrelly, T. Devic, P. A. Wright, G. de Weireld, C. Serre, G. Maurin and P. L. Llewellyn, *J. Mater. Chem. A*, 2016, **4**, 1383–1389.
103 V. Trannoy, N. Guillou, C. Livage, C. Roch-Marchal, M. Haouas, A. Leaustic, C. Allain, G. Clavier, P. Yu and T. Devic, *Inorg. Chem.*, 2019, **58**, 6918–6926.
104 M. Taddei, F. Costantino, F. Marmottini, A. Comotti, P. Sozzani and R. Vivani, *Chem. Commun.*, 2014, **50**, 14831–14834.
105 L. Samperisi, A. Jaworski, G. Kaur, K. P. Lillerud, X. Zou and Z. Huang, *J. Am. Chem. Soc.*, 2021, **143**, 17947–17952.
106 G. Mouchaham, L. Cooper, N. Guillou, C. Martineau, E. Elkaim, S. Bourrelly, P. L. Llewellyn, C. Allain, G. Clavier, C. Serre and T. Devic, *Angew. Chem., Int. Ed.*, 2015, **54**, 13297–13301.
107 J. Jacobsen, L. Wegner, H. Reinsch and N. Stock, *Dalton Trans.*, 2020, **49**, 11396–11402.
108 R. D'Amato, A. Donnadio, M. Carta, C. Sangregorio, D. Tiana, R. Vivani, M. Taddei and F. Costantino, *ACS Sustainable Chem. Eng.*, 2018, **7**, 394–402.
109 S. Leubner, R. Siegel, J. Franke, M. T. Wharmby, C. Krebs, H. Reinsch, J. Senker and N. Stock, *Inorg. Chem.*, 2020, **59**, 15250–15261.
110 M. Zhao, Y. Huang, Y. Peng, Z. Huang, Q. Ma and H. Zhang, *Chem. Soc. Rev.*, 2018, **47**, 6267–6295.
111 Y. Qin, Y. Wan, J. Guo and M. Zhao, *Chin. Chem. Lett.*, 2022, **33**, 693–702.
112 J. Guo, Y. Duan, Y. Liu, H. Li, Y. Zhang, C. Long, Z. Wang, Y. Yang and S. Zhao, *J. Mater. Chem. A*, 2022, **10**, 6463–6469.
113 J. Guo, Y. Wan, Y. Zhu, M. Zhao and Z. Tang, *Nano Res.*, 2021, **14**, 2037–2052.
114 D. Gao, J. H. Chen, S. Fang, T. Ma, X. H. Qiu, J. G. Ma, Q. Gu and P. Cheng, *Matter*, 2021, **4**, 1001–1016.
115 G. Zheng, I. Pastoriza Santos, J. Pérez Juste and L. M. Liz Marzán, *SmartMat*, 2021, **2**, 446–465.
116 X. Li, Y. Li, L. Ma, L. Hou, C. He, Y. Wang and Z. Zhu, *J. Mater. Chem. A*, 2020, **8**, 5227–5233.
117 M. F. Ghazvini, M. Vahedi, S. N. Nobar and F. Sabouri, *J. Environ. Chem. Eng.*, 2021, **9**, 104790.
118 D. Wu, P. F. Zhang, G. P. Yang, L. Hou, W. Y. Zhang, Y. F. Han, P. Liu and Y. Y. Wang, *Coord. Chem. Rev.*, 2021, **434**, 213709.
119 N. Monni, E. Andres Garcia, K. Caamaño, V. García López, J. M. Clemente Juan, M. Giménez Marqués, M. Oggianu, E. Cadoni, G. Mínguez Espallargas, M. Clemente León, M. L. Mercuri and E. Coronado, *J. Mater. Chem. A*, 2021, **9**, 25189–25195.
120 R. Lin, S. Xiang, W. Zhou and B. Chen, *Chem*, 2020, **6**, 337–363.
121 Y. Li, G. Wang, L. Ma, L. Hou, Y. Wang and Z. Zhu, *ACS Appl. Mater. Interfaces*, 2021, **13**, 4102–4109.
122 M. Xu, S. S. Yang and Z. Y. Gu, *Chem.–Eur. J.*, 2018, **24**, 15131–15142.
123 Z. Ji, T. Li and O. M. Yaghi, *Science*, 2020, **369**, 674–680.
124 J. Zhu, X. Chen, A. Q. Thang, F. L. Li, D. Chen, H. Geng, X. Rui and Q. Yan, *SmartMat*, 2022, DOI: **10.1002/smm2.1091**.
125 H. M. Mei, S. Li, J. R. Dong, L. Zhang and C. Y. Su, *ChemistrySelect*, 2020, **5**, 10988–10995.
126 Z. Wu, J. Xie, Z. J. Xu, S. Zhang and Q. Zhang, *J. Mater. Chem. A*, 2019, **7**, 4259–4290.
127 Z. Wu, D. Adekoya, X. Huang, M. J. Kiefel, J. Xie, W. Xu, Q. Zhang, D. Zhu and S. Zhang, *ACS Nano*, 2020, **14**, 12016–12026.
128 C. Li, K. Wang, J. Li and Q. Zhang, *Nanoscale*, 2020, **12**, 7870–7874.
129 X. Y. Dong, X. P. Hu, H. C. Yao, S. Q. Zang, H. W. Hou and T. C. Mak, *Inorg. Chem.*, 2014, **53**, 12050–12057.
130 J. Su, W. He, X. M. Li, L. Sun, H. Y. Wang, Y. Q. Lan, M. Ding and J. L. Zuo, *Matter*, 2020, **2**, 711–722.
131 Y. Guo, K. Wang, Y. Hong, H. Wu and Q. Zhang, *Dalton Trans.*, 2021, **50**, 11331–11346.
132 Y. Dong, S. Li, S. Hong, L. Wang and B. Wang, *Chin. Chem. Lett.*, 2020, **31**, 635–642.
133 C. Wang, X. Li, W. Yang, Y. Xu and H. Pang, *Chin. Chem. Lett.*, 2021, **32**, 2909–2913.
134 Y. Pan, R. Abazari, Y. Wu, J. Gao and Q. Zhang, *Electrochem. Commun.*, 2021, **126**, 107024.
135 H. F. Wang, L. Chen, H. Pang, S. Kaskel and Q. Xu, *Chem. Soc. Rev.*, 2020, **49**, 1414–1448.
136 X. P. Wu, L. Gagliardi and D. G. Truhlar, *J. Am. Chem. Soc.*, 2018, **140**, 7904–7912.
137 J. Gao, Q. Huang, Y. Wu, Y. Q. Lan and B. Chen, *Adv. Energy Sustain. Res.*, 2021, **2**, 2100033.
138 A. de Oliveira, G. F. de Lima and H. A. De Abreu, *Chem. Phys. Lett.*, 2018, **691**, 283–290.
139 C. Y. Wang, C. C. Wang, X. W. Zhang, X. Y. Ren, B. Yu, P. Wang, Z. X. Zhao and H. f. Fu, *Chin. Chem. Lett.*, 2022, **33**, 1353–1357.

140 X. Y. Li, Y. B. Wang, Y. Song, D. Xiang and C. z. He, *J. Inorg. Organomet. Polym. Mater.*, 2021, **31**, 3823–3828.
141 T. Maity, D. Saha, S. Das and S. Koner, *Eur. J. Inorg. Chem.*, 2012, **2012**, 4914–4920.
142 S. Halake and K. M. Ok, *J. Solid State Chem.*, 2015, **231**, 132–137.
143 Y. W. Li, J. P. Zhao, L. F. Wang and X. H. Bu, *CrystEngComm*, 2011, **13**, 6002–6006.
144 M. Sanselme, J. M. Greneche, M. Riou-Cavellec and G. Ferey, *Chem. Commun.*, 2002, **18**, 2172–2173.
145 X. Zhang, J. X. Chen and H. G. Zheng, *Inorg. Chem. Commun.*, 2016, **69**, 4–6.
146 M. Chen, Z. W. Wang, H. Zhao and C. S. Liu, *Inorg. Chem. Commun.*, 2014, **45**, 84–88.
147 Y. Hu, M. Ding, X. Q. Liu, L. B. Sun and H. L. Jiang, *Chem. Commun.*, 2016, **52**, 5734–5737.
148 H. M. Titi, G. Nandi, R. Thakuria and I. Goldberg, *Inorg. Chim. Acta*, 2015, **426**, 55–63.
149 G. E. Gomez, M. C. Bernini, E. V. Brusau, G. E. Narda, D. Vega, A. M. Kaczmarek, R. Van Deun and M. Nazzarro, *Dalton Trans.*, 2015, **44**, 3417–3429.
150 R. F. D'Vries, I. Camps and J. Ellena, *Cryst. Growth Des.*, 2015, **15**, 3015–3023.
151 M. O'Keeffe, M. A. Peskov, S. J. Ramsden and A. O. M. Yaghi, *Acc. Chem. Res.*, 2008, **41**, 1782–1789.
152 O. M. Yaghi, *Nano Lett.*, 2020, **20**, 8432–8434.
153 S. Yuan, J. Peng, B. Cai, Z. Huang, A. T. Garcia Esparza, D. Sokaras, Y. Zhang, L. Giordano, K. Akkiraju, Y. G. Zhu, R. Hubner, X. Zou, Y. Roman Leshkov and Y. Shao Horn, *Nat. Mater.*, 2022, **21**, 673–680.